A computational model for microcirculation including Fahraeus-Lindqvist effect, plasma skimming and fluid exchange with the tissue interstitium

Luca Possenti[1], Simone di Gregorio[1,2], Fannie Maria Gerosa[3], Giorgio Raimondi[2], Giustina Casagrande[1], Maria Laura Costantino[1], Paolo Zunino[2]

[1]*LaBS, Dipartimento di Chimica, Materiali e Ingegneria Chimica "Giulio Natta", Politecnico di Milano, Italy*
[2]*MOX, Department of Mathematics, Politecnico di Milano, Italy*
[3]*Inria Paris, 75012 Paris, France*

SUMMARY

We present a two phase model for microcirculation that describes the interaction of plasma with red blood cells. The model takes into account of typical effects characterizing the microcirculation, such as the Fahraeus-Lindqvist effect and plasma skimming. Besides these features, the model describes the interaction of capillaries with the surrounding tissue. More precisely, the model accounts for the interaction of capillary transmural flow with the surrounding interstitial pressure. Furthermore, the capillaries are represented as one-dimensional channels with arbitrary, possibly curved configuration. The latter two features rely on the unique ability of the model to account for variations of flow rate and pressure along the axis of the capillary, according to a local differential formulation of mass and momentum conservation. Indeed, the model stands on a solid mathematical foundation, which is also addressed in this work. In particular, we present the model derivation, the variational formulation and its approximation using the finite element method. Finally, we conclude the work with a comparative computational study of the importance of the Fahraeus-Lindqvist, plasma skimming and capillary leakage effects on the distribution of flow in a microvascular network.

*Correspondence to: *Paolo Zunino, MOX, Department of Mathematics, Politecnico di Milano paolo.zunino@polimi.it

1. INTRODUCTION

Mathematical modeling is a well accepted tool of investigation in microcirculation [35], because it complements experimental investigation by facilitating the formulation of hypotheses to be tested against real data. Mathematical models for microcirculation have evolved over the last three decades (at least), with the attempt to advance the state of art from phenomenological models to predictive ones [56]. Now, there is a fairly good agreement about the fundamental traits of models for blood flow in the microcirculation. More precisely, the importance of nonlinear blood rheology depending on hematocrit [22, 18, 38, 23, 39, 58], the role of the microvascular morphology [4, 20, 52, 19], and of the extravascular pressure gradient [16, 15], is well accepted. However, how the interaction of these essential factors determine the main features of blood flow at the microvascular level still presents some unresolved questions. For this reason, the development of mathematical and computational models able to address the complexity of these phenomena is still up to date.

From the computational standpoint, the panorama looks more scattered. This may be due to the intrinsic difficulty to solve the microcirculation problem, because it involves differential and nonlinear governing equations defined on networks of complex shape. Even though it is out of the scope of this work to provide a comprehensive review, we mention here some representative approaches, such as the one of [22, 14, 13], the method of Green's functions [28, 57], and also the approaches that look at the microvascular bed as a porous medium [63, 8, 45].

The objective of this work is to derive a model of microcirculation and its interaction with the interstitial volume, where the effect of pressure gradients is taken into account. As mentioned before, the model does also include a nonlinear blood rheology, dependent of the vessel diameter and the hematocrit, as well as it is able to account for complex vascular geometries. To include complex geometries, we adopt a mesoscale approach conceptually similar to the method of Green's functions. The unique feature of this model is to be rigorously derived from the governing equation of flow, such as mass and momentum balance in a network of leaky channels. For example, we can naturally account for the role of capillary permeability and we determine how to modify the equations in accordance to curvature of the channels. The enforcement of mass conservation at the junctions of capillary branches also emerges directly from the derivation of the model. This allows us to embed plasma skimming effects in the model. According to the classification proposed in [56], the model belongs to the category of quantitative conceptual models, with the ambition to facilitate the migration of the state of art towards predictive models. The resulting mathematical problem consists of coupled partial differential equations (PDEs) on manifolds with heterogeneous dimensionality. Namely, it couples a flow and transport problem in one-dimension (1D) with a porous media flow problem in three-dimensions (3D). This approach was originally proposed in [9, 11, 10]. Besides

its relevance to applications, it has recently attracted the attention of several researchers from the perspective of mathematics. Indeed, it requires particular attention to prove existence of a solution in the weak (or variational) sense [31, 44, 32, 62].

This study is organized as follows. In the first section we present the derivation of the governing equations of flow through a vascular network of one-dimensional channels from the general three-dimensional formulation of the Navier-Stokes equations for incompressible fluids. Once the general framework is developed, we make it specific to microcirculation by introducing an additional transport equation for hematocrit, (defined as a continuum quantity, as red blood cells can not be described as individual particles at this level of detail) in virtue of which the model becomes genuinely two-phase. Also the Fahraeus-Lindqvist and plasma skimming effects are embedded into the governing principles. In the third section, we rigorously address the variational formulation of the problem, in preparation of the numerical discretization based on the finite element method. Finally, this section is concluded with the study of a numerical solution strategy to address the nonlinearity arising from the complex blood rheology. The work ends with an extended series of numerical tests with increasing level of complexity. For validation purposes, we begin from the analysis of a single vascular branch, for which the analytical solution is known. Then, we consider the flow through a Y-shaped bifurcation, to investigate the role of curvature and radius on the flow split. Finally we address a more complex network, built on the basis of a biomimetic principle related to Voronoi tassellations [54, 55].

In perspective, this work proposes a quantitative tool for the investigation of many pathologies related to microcirculation. Ongoing applications to nephrology (precisely the study of perturbed fluid homeostasis in uremic patients [47]), neurology (see for example recently published works [37, 61]) and oncology (for better understanding the microenvironment of vascularized tumors [42, 43]) are already in progress.

2. A TWO PHASE MODEL OF MICROCIRCULATION COUPLED WITH INTERSTITIAL FLOW

We define a mathematical model for fluid transport in a permeable biological tissue perfused by a capillary network. We consider a domain Ω that is composed by two parts, Ω_v and Ω_t, the capillaries and the tissue interstitium, respectively. Assuming that the capillaries can be described as cylindrical vessels, we denote with Γ the outer surface of Ω_v, with R its radius and with Λ the centerline of the capillary network. Any physical quantity of interest, such as the blood pressure p and the blood velocity u, is a function of space (being $x \in \Omega$ the spatial coordinates). We consider steady-state

flow conditions, as a result all variables are independent of time. The flow model in the vascular domain Ω_v reads as follows:

$$
\begin{cases}
\nabla \cdot \boldsymbol{u}_t = 0 & \text{in } \Omega_t \\[2mm]
\boldsymbol{u}_t + \dfrac{\mathrm{K}}{\mu_t}\nabla p_t = 0 & \text{in } \Omega_t \\[2mm]
\rho\dfrac{\partial \boldsymbol{u}_v}{\partial t} + \rho(\boldsymbol{u}_v \cdot \nabla)\boldsymbol{u}_v = \nabla \cdot \boldsymbol{\sigma} & \text{in } \Omega_v \\[2mm]
\nabla \cdot \boldsymbol{u}_v = 0 & \text{in } \Omega_v
\end{cases}
\tag{1}
$$

where $\boldsymbol{\sigma}(\boldsymbol{u}_v, p_v) = 1/2\mu_v(\nabla\boldsymbol{u}_v + \nabla^T\boldsymbol{u}_v) - \nabla p_v$ is the Cauchy stress in the blood and μ_v is the apparent (or effective) blood viscosity. In addition, μ_t and K denote the dynamic fluid viscosity and the hydraulic permeability of the interstitial tissue, respectively, and ρ is the blood density. The viscosity of the interstitial fluid, μ_t, is taken from [60]. It is comparable to the one of blood plasma at body temperature of 37°, which will be later denoted by μ_{ref} (we remand to Table I for the values of the parameters and corresponding references). At the interface $\Gamma = \partial\Omega_v \cap \partial\Omega_t$ we impose continuity of the flow:

$$
\boldsymbol{u}_v \cdot \boldsymbol{n} = \boldsymbol{u}_t \cdot \boldsymbol{n} = f(p_t, p_v) \text{ with } f(p_t, p_v) = L_p\big((p_v - p_t) - (\pi_v - \pi_t)\big), \quad \boldsymbol{u}_t \cdot \boldsymbol{\tau}_k = 0, \quad \text{on } \Gamma
\tag{2}
$$

where $\boldsymbol{n}$ is the outward unit vector normal to the capillary surface and $\boldsymbol{\tau}_k$, $k = 1, 2$ are the tangential and binormal vectors. The fluid flux across the capillary wall can be obtained on the basis of linear non-equilibrium thermodynamic arguments, originally developed by Kedem and Katchalsky. In particular L_p is the hydraulic conductivity of the vessel wall, R_g is the universal gas constant and T is the absolute temperature. In (2) π_v and π_t determine the osmotic (or oncotic) pressure gradient across the capillary wall, namely $\delta\pi = \pi_v - \pi_t$, due to the difference in the concentration of proteins (for example albumin), [33]. In what follows, we assume that $\delta\pi$ is given and is independent of $\boldsymbol{x}$.

2.1. Derivation of the governing flow equations in a capillary with arbitrary geometry

The one dimensional model that governs the bulk flow in each branch of a generic microcirculation network is obtained as follows. Let us define a local cylindrical coordinate system $\boldsymbol{x} = (r, \theta, s)$ at each point of the centerline of the capillaries. We denote with $\boldsymbol{e}_r, \boldsymbol{e}_\theta, \boldsymbol{e}_s$ the radial, circumferential and axial unit vectors. The model is based on the following, geometric, kinematic and dynamic assumptions:

Circular section For each value of the arc length s along a network branch, the intersection between the orthogonal plan to $\boldsymbol{e}_s$ and the vessel is circular.

Dominance of axial velocity The radial and circumferential velocity components are negligible compared to the axial component, namely $\boldsymbol{u}_v = [0, 0, u_v(r, \theta, s)]^T$.

Body forces We neglect the effect of gravity and other possible types of body forces (inertia, Coriolis).

Steady flow We neglect transient phenomena. Microcirculation is characterized by negligible fluctuations of the blood pressure due to the heartbeat, namely the Womersley numbers at the level of capillary circulation are negligible [24]. For this reasons, we just aim to determine the steady flow conditions.

Dominance of viscous forces Microcirculation is also characterized by the dominance of viscous forces over inertial forces acting on infinitesimal fluid particles, namely the Reynolds number characterizing the flow is low.

Viscosity We assume that the apparent viscosity of blood, μ_v is independent of the local deformation rate conditions. However, the viscosity is not a constant parameter but it depends on the hematocrit and on the vessel radius.

Under these assumptions the mass balance and momentum equations governing an incompressible flow, such as blood, reduce to the following form,

$$u_r = u_\theta = 0, \partial_r p_v = 0, \; \partial_\theta p_v = 0, \; \partial_s u_v = 0, \; -\mu_v \Delta u_v + \partial_s p = 0, \tag{3}$$

for any $(r, \theta, s) \in \Omega_v$ where Δ denotes the Laplace operator with respect to cylindrical coordinates $\Delta u = 1/r \partial_r (r \partial_r u) + 1/r^2 \partial_\theta^2 u + \partial_s^2 u$. We now aim to transform equation (3) into a simpler one that is defined on the centerline of the capillary, solely. To this purpose, we introduce a parametrization of each curvilinear branch. Let $\boldsymbol{\Psi} : \mathbb{R} \to \mathbb{R}^3$ be the parametric arc length, such that $\boldsymbol{\Psi} \in C^3(\mathbb{R})$ and $\|d_z \boldsymbol{\Psi}(z)\| = 1$ for any $z \in [0, L]$ being L the length of a generic branch of the capillary network. Note that $s = \int_0^z \|d_\zeta \boldsymbol{\Psi}(\zeta)\| d\zeta = z$. The curvature of the arc at a specific location, is $\kappa = \|d_{zz} \boldsymbol{\Psi}(z)\|$; the centripetal unitary direction is $\boldsymbol{N} = d_{zz} \boldsymbol{\Psi}(z)/\kappa$ and the center C_0 of the osculating circle is the point in the direction $\boldsymbol{N}(z)$ with distance $1/\kappa$ from $\boldsymbol{\Psi}(z)$.

In order to proceed with the one-dimensional model derivation, we set the following ansatz: *the axial velocity profile can be decomposed as $u_v(r, \theta, s) = \overline{u}_v(s)\Phi(r, \theta)$ where $\overline{u}_v$ represents the mean*

or bulk velocity of the blood stream on the cross section identified by the arc length s, denoted by $\Sigma(s)$. More precisely, in what follows we will use the notation

$$\overline{u}_v(s) = \frac{1}{\pi R^2} \int_{\Sigma(s)} u_v \, d\sigma \,, \quad \overline{p}_v(s) = \frac{1}{\pi R^2} \int_{\Sigma(s)} p_v \, d\sigma \,, \quad \overline{\overline{p}}_t(s) = \frac{1}{2\pi R} \int_{\partial\Sigma(s)} p_t \, d\sigma \,,$$

where $\overline{\overline{p}}_t$ is the mean interstitial pressure on the boundary of a section Σ. The function $\phi(r, \theta)$ is a shape factor that is represented as

$$\Phi(r, \theta) = \phi(r/R)(1 + ar\cos\theta + br\sin\theta + cr^2\cos\theta\sin\theta + dr^2\cos^2\theta + er^2\sin^2\theta)\,, \qquad (4)$$

where a, b, c, d, e are parameters to be determined in what follows. The radially symmetric part of the profile, namely $\phi(r/R)$ is usually modeled as,

$$\phi(\rho) = \frac{\gamma + 2}{\gamma}\left(1 - \rho^\gamma\right),$$

which coincides with the classic Poiseuille parabolic flow profile (observed in straight cylindrical channels) for $\gamma = 2$.

We aim to find a suitable expression for the parameters a, b, c, d, e in terms of the geometry of the centerline, namely $\boldsymbol{\Psi}$, such that the shape factor coincides with the classic parabolic Poiseuille profile when the centerline is rectilinear, while it deviates from this pattern when the centerline is curved. To this purpose, we set the following additional assumptions:

Choice of θ We assume that on each cross section the axis $\theta = 0$ is colinear with the vector $\mathbf{N}$.

Symmetry of the profile We require that the velocity profile in each section is such that $\Phi(r, \theta, \psi) = \Phi(r, -\theta, \psi) \quad \forall r, \theta, \psi$. As a result of that the coefficient b, c must vanish, namely $b = c = 0$.

Linear dependence We assume that the correction factor of the velocity profile at any point s, namely $(1 + ar\cos\theta + br\sin\theta + cr^2\cos\theta\sin\theta + dr^2\cos^2\theta + er^2\sin^2\theta)$ is linearly dependent of the distance from the center of the osculating circle relative to this point.

We are now able to determine the coefficients a, d, e which satisfy these assumptions. For the linear dependence of the velocity with the distance from the center of the osculating circle, our profile must be zero in $C_0 = (r = 1/\kappa, \theta = 0, \psi)$, that is $(1 + a/\kappa + d/\kappa^2) = 0 \rightarrow d = -a\kappa - \kappa^2$. Furthermore, since the velocity profile is linearly dependent to the distance from the center of the osculating circle, we have that all the points with distance $1/\kappa$ from it must have the same velocity.

The set of points of each cross section with distance $1/\kappa$ from the point C_0 are:

$$\varphi = \{(r,\theta): \quad r = \frac{2\cos\theta}{\kappa}, \quad \theta \in [-\frac{\pi}{2}; +\frac{\pi}{2}]\}.$$

Moreover we have that $\Phi(r=0,\theta,\psi) = \phi(0)$ and so $\forall (r,\theta) \in \phi$ then $\Phi(r,\theta,\psi) = \phi(r/R)$. It follows that $\forall (r,\theta) \in \varphi$:

$$0 = ar\cos\theta + dr^2\cos^2\theta + er^2\sin^2\theta = 2\frac{a}{\kappa}\cos^2\theta + 4\frac{d}{\kappa^2}\cos^4\theta + 4\frac{e}{\kappa^2}\cos^2\theta\sin^2\theta.$$

Now for $\theta = \pm\frac{\pi}{2}$ the equation is verified. In the other cases we can divide all by $2\cos^2\theta/\kappa^2$, to obtain:

$$0 = a\kappa + 2d\cos^2\theta + 2e\sin^2\theta \qquad \forall \theta \in \left(-\frac{\pi}{2}, +\frac{\pi}{2}\right).$$

To find the value of the parameters we need two more equations. Thus, we test it on two particular cases: $\theta = \pi/4, \theta = \pi/3$. For $\theta = \pi/4$, using $d = -a\kappa - \kappa^2$ we obtain:

$$0 = a\kappa + 2d(\frac{1}{2}) + 2e(\frac{1}{2}) = a\kappa + d + e = a\kappa - \kappa^2 - a\kappa + e = e - \kappa^2.$$

For that $e = \kappa^2$. Finally for $\theta = \pi/3$, using the previous result we have:

$$0 = a\kappa + 2d(\frac{1}{4}) + 2e(\frac{3}{4}) = a\kappa + \frac{d}{2} + \frac{3e}{2} = a\kappa - \frac{\kappa^2}{2} - \frac{a\kappa}{2} + \frac{3\kappa^2}{2} = \frac{a\kappa}{2} + \kappa^2$$

So we obtain $a = -2\kappa$ and $d = \kappa^2$. In a general configuration the curvature is dependent on the arc length $\kappa = \kappa(s)$. In conclusion, the velocity profile is of the form:

$$\Phi(r,\theta,\psi) = \phi(rR^{-1})(1 + r^2\kappa^2(\psi) - 2\kappa(\psi)r\cos\theta). \tag{5}$$

A visualization of such profile is provided in Figure 1

Now we derive the reduced model for flow in curved vessels by replacing the velocity profile (5) into the mass and momentum balance equations (3) and we integrate these equations on a portion of vessel, P delimited by two cross sections $\Sigma(s_1), \Sigma(s_2), \ s_2 > s_1$. In this way, we obtain simplified equations that depend only on the arc length s. We start first from the continuity equation, using the
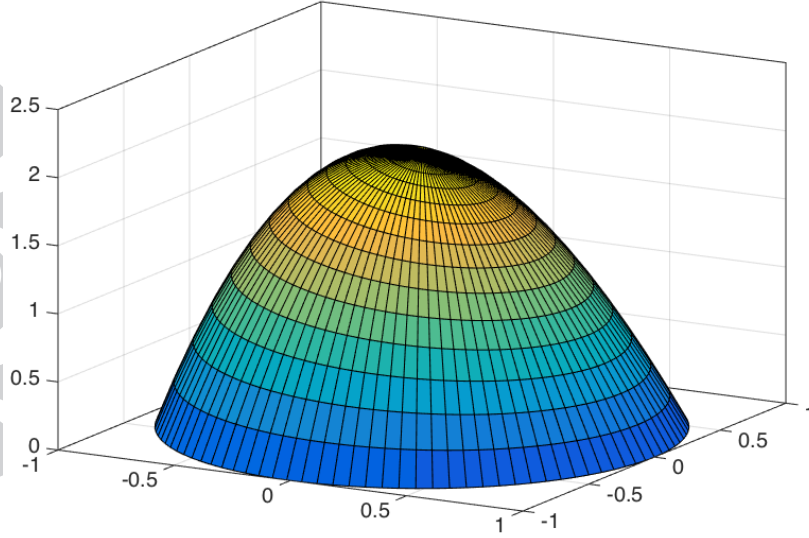
Figure 1. Visualization of the dimensionless velocity profile for a curved pipe obtained using expression (5). The shape parameter is $\gamma = 2$ and the curvature is such that $\kappa R = 0.11$ as in the numerical simulations.

fact that $\boldsymbol{n} = \boldsymbol{e}_s$ on $\Sigma(s_1)$ and $\Sigma(s_2)$ we obtain:

$$0 = \int_P \nabla \cdot \boldsymbol{u}_v d\Omega = \int_{\partial P} \boldsymbol{u}_v \cdot \mathbf{n} \, d\sigma = \int_{\Sigma(s_1)} \boldsymbol{u}_v \cdot \boldsymbol{n} d\sigma + \int_{\Sigma(s_2)} \boldsymbol{u}_v \cdot \boldsymbol{n} \, d\sigma + \int_{\Gamma} \boldsymbol{u}_v \cdot \boldsymbol{n} \, d\sigma$$

$$= -\int_{\Sigma(s_1)} u_v \, d\sigma + \int_{\Sigma(s_2)} u_v \, d\sigma + \int_{\Gamma} f(p_t, p_v) \, d\sigma \simeq -\overline{u}_v(s_1)\pi R^2(s_1) + \overline{u}_v(s_2)\pi R^2(s_2) + \int_{s_1}^{s_2} f(\overline{p}_t, p_v) dz$$

$$= \int_{s_1}^{s_2} [f(\overline{\overline{p}}_t, \overline{p}_v) + \partial_s(\pi R^2 \overline{u}_v)] dz \,.$$

$$(6)$$

According to (3), in particular $\partial_r p_v = \partial_\theta p_v = 0$, we notice that $p_v(r, s, \theta) = \overline{p}_v(s)$. Furthermore, in equation (6) we have adopted the assumption that the radius of the capillary is small if compared to the domain Ω. More precisely, we have set that

$$\int_{\Gamma} f(p_t, p_v) \, d\sigma = \int_{s_1}^{s_2} \int_0^{2\pi} f(p_t, p_v) R(s) d\theta \, ds = \int_{s_1}^{s_2} \int_0^{2\pi} f(p_t, \overline{p}_v) R(s) d\theta \, ds = \int_{s_1}^{s_2} 2\pi R(s) f(\overline{\overline{p}}_t, \overline{p}_v) \, ds \,,$$

where the last step holds true because $f(p_t, p_v)$ is a linear function of its arguments.

Let us now apply the averaging technique to the momentum balance equation, that is the last of (3). We have:

$$\int_P \Delta u_v \, d\Omega = \int_{\partial P} \nabla u_v \cdot \boldsymbol{n} \, d\sigma = -\int_{\Sigma(s_1)} \partial_s u_v \, d\sigma + \int_{\Sigma(s_2)} \partial_s u_v \, d\sigma + \int_{\Gamma} \nabla u_v \cdot \boldsymbol{n} \, d\sigma = \int_{\Gamma} \nabla u_v \cdot \boldsymbol{e}_r \, d\sigma$$

$$= \int_{\Gamma} \partial_r u_v d\sigma = \int_{\Gamma} \overline{u}_v(s) \partial_r \Phi(r, \theta) d\sigma = \int_{\Gamma} \overline{u}_v(s) R^{-1} \phi'(rR^{-1})(1 - 2\kappa r \cos\theta + \kappa^2 r^2) + \phi(rR^{-1})(2\kappa^2 r - 2\kappa \cos\theta) \, d\sigma$$

$$= \int_{s_1}^{s_2} \int_0^{2\pi} \overline{u}_v(s) \big(R^{-1} \phi'(1)(1 - \kappa \cos\theta + \kappa^2 R^2) + \phi(1)(2\kappa^2 R - 2\kappa \cos\theta) \big) R d\theta ds.$$

Now using the fact that $\phi(1) = 0$, the periodicity of $\cos\theta$, we obtain:

$$\int_P \Delta u_v \, d\Omega = \int_{s_1}^{s_2} 2\pi\phi'(1)(1 + \kappa^2 R^2)\overline{u}_v(s) \, ds,$$

such that the averaged/one-dimensional form of the momentum equation becomes

$$-2\pi\mu_v(s)\phi'(1)\big(1 + \kappa^2(s)R^2\big)\overline{u}_v(s) + \pi R^2 \partial_s \overline{p}_v(s) = 0.$$

2.2. *Extension to a network of capillaries*

Now that we have derived the 1D model equations we need to generalize them to a more complex topology. To this purpose, we decompose the network in Λ_i branches, $i = 1, ..., N$. The branches are parametrized by the arc length s_i; a tangent unit vector $\boldsymbol{\lambda}_i$ is also defined over each branch, accounting for an arbitrary branch orientation. Differentiation over the branches is defined using the tangent unit vector, namely $\partial_{s_i} := \boldsymbol{\lambda}_i \cdot \nabla$ on Λ_i, i.e. ∂_{s_i} represents the projection of ∇ along $\boldsymbol{\lambda}_i$. So far, the equations that govern the flow in each branch of the network are uncoupled. In order to make the flow problem fully coupled we need to enforce constraints at the junctions of the branches. Junctions are defined as the points $\boldsymbol{y}$ such that

$$\boldsymbol{y}_j = \boldsymbol{\Psi}_i(s_i^*) = \boldsymbol{\Psi}_{\hat{i}}(s_{\hat{i}}^*), \; s_i^* \in \{0, L_i\} \; \forall i, \hat{i} = 1, \dots, N$$

Let us count the junctions with the index $j = 1, 2, \ldots, M$ and let us denote with $\mathcal{K}_j$ the set of indices i such that $\boldsymbol{\Psi}_i(s_i^*) = \boldsymbol{y}_j$. These are the branches that join at the j-th junction. There may be branches that end inside or at the boundary of the domain Ω. The former are said *dead ends* and are denoted with $\boldsymbol{z}$. The indices of branches featuring a dead end are $i \in \mathcal{E}$. The latter points are called *boundary ends* and are identified by the symbol $\boldsymbol{x}$. The set of branches intersecting the outer boundary is $i \in \mathcal{B}$.

The branches that merge at the j-th junction can be subdivided according to different criteria. We present here two options, both useful later on. Let $\boldsymbol{\lambda}_i$ be the orientation of a given branch of the network and let $\boldsymbol{e}_s$ be the *outgoing* tangential unit vector at the each of the two endpoints of the branch, identified respectively by the arc length coordinates $s_i = 0$ and $s_i = L$.

The *ingoing points* are identified by the following conditions: $\boldsymbol{\lambda}_i \cdot \boldsymbol{e}_s(s_i) < 0$ for $s_i = 0$ and $s_i = L$. The *outgoing* points are obviously the ones such that $\boldsymbol{\lambda}_i \cdot \boldsymbol{e}_s(s_i) > 0$. The indices i that correspond to ingoing branches at the j-th junction are denoted with $\mathcal{K}_j^-$, while the indices of the outgoing branches at the junction are collected in $\mathcal{K}_j^+$.

If we add the orientation of the flow to this classification we obtain that the *inflow points* are identified by the following condition that involves the orientation of the flow: $\overline{u}_v(s_i)\boldsymbol{\lambda}_i \cdot \boldsymbol{e}_s(s_i) < 0$

for $s_i = 0$ and $s_i = L$. The *outflow* points are obviously the ones such that $\overline{u}_v(s_i)\boldsymbol{\lambda}_i \cdot \boldsymbol{e}_s(s_i) > 0$. The corresponding indices are collected in the sets $\mathcal{K}_j^{in}$, $\mathcal{K}_j^{out}$, respectively. We classify similarly the boundary ends, subdividing the points $\boldsymbol{x}$ into ingoing or outgoing, namely $\boldsymbol{x}^-, \boldsymbol{x}^+$, or into inflow and outflow $\boldsymbol{x}^{in}, \boldsymbol{x}^{out}$. At these points, we set the vascular pressure equal to a prescribed value $\overline{p}_v(\boldsymbol{x}_i) = g_v(\boldsymbol{x}_i)$, $i \in \mathcal{B}$, while the value of hematocrit will be enforced at the inflow points solely, $\boldsymbol{x}^{in}$.

We enforce balance of flow rates and continuity of pressure at each junction, namely,

$$\sum_{i \in \mathcal{K}_j} \pi R_k^2 \overline{u}_{v,i} = 0, \; j = 1, 2, \ldots, M, \quad \overline{p}_{v,i} = \overline{p}_{v,\hat{i}}, \; i, \hat{i} \in \mathcal{K}_j, \; j = 1, 2, \ldots, M.$$

At dead ends of the network we set no-flow conditions $\pi R^2 \overline{u}_v|_{\boldsymbol{z}_i} = 0$, $i \in \mathcal{E}$, where $|_{\boldsymbol{z}_i}$ is a shorthand notation for the evaluation of a function (or better the whole term) in the point $\boldsymbol{z}_i$.

In conclusion, the coupled model of blood flow in the network is the following,

$$\begin{cases} \partial_s\left(\pi R_i^2(s)\overline{u}_{v,i}(s)\right) + 2\pi R_i(s) f(\overline{\overline{p}}_t(s), \overline{p}_v(s)) = 0 & \text{on } \Lambda_i, \; i = 1, \ldots, N, \\[2mm] -2\mu_{v,i}(s)\phi'(1)\left(1 + \kappa_i^2(s)R_i^2(s)\right)\overline{u}_{v,i}(s) + R_i^2(s)\partial_s\overline{p}_{v,i}(s) = 0 & \text{on } \Lambda_i, \; i = 1, \ldots, N, \\[2mm] \sum_{i \in \mathcal{K}_j} \pi R_k^2 \overline{u}_{v,i}|_{\boldsymbol{y}_j} = 0 & j = 1, 2, \ldots, M, \\[2mm] \overline{p}_{v,i}|_{\boldsymbol{y}_j} = \overline{p}_{v,\hat{i}}|_{\boldsymbol{y}_j} & i, \hat{i} \in \mathcal{K}_j, \; j = 1, 2, \ldots, M, \\[2mm] \pi R^2 \overline{u}_v|_{\boldsymbol{z}_i} = 0 & i \in \mathcal{E}, \\[2mm] \overline{p}_v|_{\boldsymbol{x}_i} = g_v & i \in \mathcal{B}. \end{cases} \tag{7}$$

We notice that in the case of a straight, cylindrical, impermeable pipe, i.e. $\gamma = 2$, the coefficient $\phi'(1) = -4$ and $f(\overline{\overline{p}}_t, \overline{p}_v) = 0$, such that these equations coincide with the standard Poiseuille flow.

Finally, we address the coupling of the reduced model (7) with the porous media equation in the surrounding environment, as described in (1). We follow the approach proposed in [6], where the interaction of the manifold Λ with the bulk domain Ω is represented by means of the distribution of concentrated sources on Λ. Owing to these assumptions, we identify Ω_t with Ω and we introduce a new term on the left hand side to the first equation of (1). To guarantee mass conservation, this new term must be opposite to $f(\overline{\overline{p}}_t(s), \overline{p}_v(s))$ and be multiplied by δ_{Λ_i} that is a distribution of Dirac

masses along the manifold Λ_i. As a result of that, the flow model that describes capillaries as one-dimensional channels coupled with a porous interstitial tissue reads as follows:

$$
\begin{cases}
\nabla \cdot \boldsymbol{u}_t - 2\pi R(s) f(\overline{\overline{p}}_t(s), \overline{p}_v(s)) \delta_\Lambda = 0 & \text{in } \Omega \\[2mm]
\boldsymbol{u}_t + \frac{\mathrm{K}}{\mu_t} \nabla p_t = 0 & \text{in } \Omega \\[2mm]
\partial_s \big(\pi R_i^2(s) \overline{u}_{v,i}(s)\big) + 2\pi R_i(s) f(\overline{\overline{p}}_t(s), \overline{p}_v(s)) = 0 & \text{on } \Lambda_i,\ i = 1, \ldots, N\,, \\[2mm]
-2\mu_{v,i}(s)\phi'(1)\big(1 + \kappa_i^2(s) R_i^2(s)\big) \overline{u}_{v,i}(s) + R_i^2(s) \partial_s \overline{p}_{v,i}(s) = 0 & \text{on } \Lambda_i,\ i = 1, \ldots, N\,, \\[2mm]
\sum_{i \in \mathcal{K}_j} \pi R_k^2 \overline{u}_{v,i}|_{\boldsymbol{y}_j} = 0, & j = 1, 2, \ldots, M\,, \\[2mm]
\overline{p}_{v,i}|_{\boldsymbol{y}_j} = \overline{p}_{v,\hat{i}}|_{\boldsymbol{y}_j} & i, \hat{i} \in \mathcal{K}_j,\ j = 1, 2, \ldots, M\,, \\[2mm]
\pi R^2 \overline{u}_v|_{\boldsymbol{z}_i} = 0 & i \in \mathcal{E}\,, \\[2mm]
\overline{p}_v|_{\boldsymbol{x}_i} = g_v & i \in \mathcal{B}\,.
\end{cases}
\tag{8}
$$

2.3. Modeling the Fahraeus-Lindqvist and the plasma skimming effects

The *apparent* (or *effective*) viscosity of blood flowing through very small channels is not constant. The main factor that affects the apparent viscosity of blood is the volumetric concentration of red blood cells, namely the *hematocrit*. Several phenomenological models are available to quantify this dependence, we refer here to a widely used one, proposed in [50]:

$$
\frac{\mu_v}{\mu_{ref}} = \left[1 + \left(\frac{\mu_{0.45}}{\mu_{ref}} - 1\right) \cdot \frac{(1-H)^C - 1}{(1-0.45)^C - 1} \cdot \left(\frac{D}{D-1.1}\right)^2\right] \cdot \left(\frac{D}{D-1.1}\right)^2
\tag{9}
$$

where H is the *discharge hematocrit*, defined such that $\pi R^2(s) \overline{u}_v(s) H(s)$ is the total flow of red blood cells that crosses a section $\Sigma(s)$ of a capillary. In the expression (9), C is a parameter depending on the diameter $D = 2R$ of the capillary:

$$
C = (0.8 + e^{-0.075D}) \cdot \left(-1 + \frac{1}{1 + 10^{-11} D^{12}}\right) + \frac{1}{1 + 10^{-11} D^{12}}
\tag{10}
$$

and $\mu_{0.45}$ is a nominal value viscosity, related to the value at 45% hematocrit,

$$
\frac{\mu_{0.45}}{\mu_{ref}} = 6 \cdot e^{-0.085D} + 3.2 - 2.44 \cdot e^{-0.06 D^{0.645}}.
\tag{11}
$$

The reference viscosity μ_{ref} is obtained from the dynamic viscosity of water (H_2O, see the IAPWS standards) as follows

$$
\mu_{ref} = 1.8 \mu_{H_2O} = 1.8 \frac{\mu_0}{1 + 0.0337T + 0.00022T^2}.
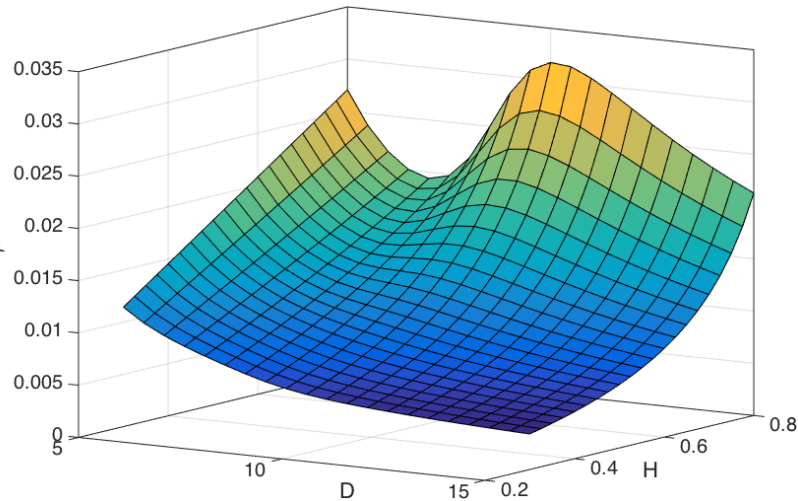\tag{12}
$$

Figure 2. Visualization of the effective viscosity (measured in $Pa \cdot s$), calculated with expression (9), in terms of the hematorit (H, %) and the capillary diameter (D, measured in microns, μm).

where T is the temperature (measured in Celsius) and $\mu_0 = 1.808$ centi-Poise (cP) is the viscosity of water at 0 C^o. The variation of the apparent viscosity, for a suitable range of hematocrit and capillary diameter is visualized in Figure 2. The model (9) entails the need to model the dynamics of hematocrit in the microvascular network. To this purpose, we propose a one-dimensional model for transport of hematocrit that will be coupled to (8). This model is set on the following assumptions.

Steady flow conditions   As we did for the bulk flow model, we study the hematocrit distribution in steady conditions.

Transport dominated regime   Let us analyze the Péclét number that characterizes the hematocrit transport,

$$Pe = \frac{LU}{D_{RBC}} \tag{13}$$

where $L \simeq 10^{-5}m$ is the RBC characteristic scale (also comparable with the capillary diameter), $U \simeq 10^{-3}m/s$ is the average velocity of RBC in the capillaries and $D_{RBC} \simeq 10^{-12}m^2/s$ is the diffusivity parameter of RBC in water [3, 26, 46]. As a result we obtain $Pe \simeq 10^4$ that justifies the assumption of advection dominated RBC transport.

Reactions and leak off   We assume that the RBC do not leak off from the capillaries and we neglect any effects involving production or sequestration of RBC from the blood stream.

Absence of trifurcations at network junctions   We assume that all the inner junctions of the network can be classified either as *anastomoses* or *bifurcations*.

On the basis of these hypotheses, the dynamics of hematocrit in a capillary network, where each capillary branch is modeled as a one-dimensional channel, is described by the mass balance equation. Denoting the flow rate of hematocrit across a single channel as Q_H, owing to the definition of discharge hematocrit we directly have $Q_H = \pi R^2 \overline{u}_v H$ and the mass balance equation for hematocrit becomes,

$$\partial_s\left(\pi R_i^2 \overline{u}_{v,i} H_i\right) = 0 \text{ on } \Lambda_i, \ i = 1, 2, \ldots, N. \tag{14}$$

Equation (14) will be taken as the governing equation for hematocrit in each branch of the capillary network. We observe that this equation can be easily combined with the first of (8) to obtain

$$\pi R_i^2 \overline{u}_{v,i} \partial_s H - 2\pi R_i f(\overline{\overline{p}}_t, \overline{p}_v) H_i(s) = 0 \text{ on } \Lambda_i, \ i = 1, 2, \ldots, N.$$

It shows that the hematocrit distribution is not constant along the axis of the branch, despite we neglect RBC reactions and leak off. However, hematocrit varies because the plasma can leak off and consequently the volumetric concentration of RBC may vary.

Equation (14) is not sufficient to uniquely determine the value of hematocrit in the network. It must be combined with suitable conditions for conservation of hematocrit at the junctions and at the boundary of the network. As (14) is a pure transport equation, it is well known that we have to prescribe a constraint on hematocrit at each *inflow* point of the network branches. Let us denote by $\partial \Lambda_{in}$ the inflow points at the boundary of the network. On all these points we enforce a given value of hematocrit, namely $H = H_0$ on $\partial \Lambda_{in}$. For the *internal junctions* we exploit mass conservation of hematocrit. Let us consider a generic junction with multiple branches joining at a single node. Given the orientation of the flow, we subdivide the branches into $K_{out} = \text{card}(\mathcal{K}_j^{out})$ outflow ones and $K_{in} = \text{card}(\mathcal{K}_j^{in})$ inflow branches. We prescribe as many constraints as the number of inflow branches, namely K_{in}. Mass conservation always provides one constraint that is,

$$\sum_{i \in \mathcal{K}_j^{out}} \pi R_i^2 \overline{u}_{v,i} H_i = \sum_{i \in \mathcal{K}_j^{in}} \pi R_i^2 \overline{u}_{v,i} H_i.$$

The previous equation is not sufficient to close the problem in the case $K_{in} > 1$. The simple case $K_{in} = 1$ identifies anastomoses, where one, two or multiple outflow branches merge into a sigle inflow one. In this case, since all the terms on the left hand side are known, hematocrit value on the right is uniquely determined. In case of bifurcations, namely $K_{in} = 2$, the problem can be solved by means of the flow split model proposed in [49]. Since we exclude the presence of trifurcations or more complex configurations, this approach will be entirely sufficient to determine the distribution of hematocrit in the network. Without loss of generality, let us consider the classic Y-shaped configuration, where one channel divides into two branches. We denote by the subscript f

the quantities related to the parent channel and with α, β the daughter branches. Given the blood flow rates $Q_* = \pi R_*^2 \bar{u}_{v,*}$ with $* = f, \alpha, \beta$ and the outflow hematocrit H_f, we aim to determine H_α and H_β, which provide hematocrit values at the inflow of the bifurcation branches. Using the approach of [49] we define,

$$F_{QB\alpha} = \frac{Q_\alpha}{Q_f} \quad F_{QE\alpha} = \frac{Q_\alpha H_\alpha}{Q_f H_f},$$

and we calculate these fractions by means of the following model

$$\begin{cases} F_{QE\alpha} = 0 & if \ F_{QB\alpha} \leq X_0 \\[3ex] \text{logit}(F_{QE\alpha}) = A + B\text{logit}(\frac{F_{QB\alpha} - X_0}{1 - 2X_0}) & if \ X_0 < F_{QB\alpha} < 1 - X_0 \\[3ex] F_{QE\alpha} = 1 & if \ F_{QB\alpha} \geq 1 - X_0 \end{cases}$$

where A, B are fixed parameters determined in [50], $\text{logit}(x) = \ln[x/(1 - x)]$ and X_0 is the fractional blood flow rate under which any RBC will flow into the daughter branch α. Finally, the desired hematocrit levels are determined as

$$H_\alpha = F_{QE\alpha} H_f Q_f / Q_\alpha, \quad H_\beta = (1 - F_{QE\alpha}) H_f Q_f / Q_\beta.$$

3. MATHEMATICAL FORMULATION AND NUMERICAL APPROXIMATION

3.1. Weak formulation of the two phase flow problem

For the variational formulation of the coupled flow problem (8), we proceed as previously described in [44] for a similar case. We adopt the standard notation for function spaces, see for example [51, 2]. Let's multiply the Darcy equations of (8) by test functions $q_t \in Q_t = L^2(\Omega)$, $\boldsymbol{v}_t \in \boldsymbol{V}_t = \boldsymbol{H}_{div}(\Omega)$. Owing to Green's formula we have

$$\left(\nabla p_t, \boldsymbol{v}_t \right)_\Omega = -\left(p_t, \nabla \cdot \boldsymbol{v}_t \right)_\Omega + \left(p_t, \boldsymbol{v}_t \cdot \boldsymbol{n}_t \right)_{\partial\Omega} = -\left(p_t, \nabla \cdot \boldsymbol{v}_t \right)_\Omega + \left(g_t, \boldsymbol{v}_t \cdot \boldsymbol{n}_t \right)_{\partial\Omega}$$

where g_t is a prescribed value of the interstitial pressure at the artificial boundaries of the tissue slab, namely $\partial\Omega$. For the network, we multiply the third equation of (8) by a test function $q_v \in Q_v$. In general, it is sufficient that $Q_v \subset L^2(\Lambda)$, but we require that the pressure is continuous at the junctions, according to the last equation of (8). Let $q_v|_{\boldsymbol{y}_j}$ be the uniquely defined value of q_v at the location of the j-th junction. We weakly enforce the flow rate compatibility constraints at the junctions, by multiplying the fifth equation of (8) by $q_v|_{\boldsymbol{y}_j}$ and we add it to the third equation.

In this way, we obtain the third equation of (15). To derive the last equation of (15), we multiply the fourth equation of (8) by a test function $v_{v,i} \in V_{v,i} \in H^1(\Lambda_i)$ and by πR_i^2. Then, we sum the contribution of each branch of the network. Moreover, using again Green's formula, we transfer the spatial derivative from the pressure to the test function, as follows,

$$\sum_i \left(\partial_s \overline{p}_{v,i}, \pi R_i^2 v_{v,i} \right)_{\Lambda_i} = -\sum_i \left(\overline{p}_{v,i}, \partial_s(\pi R_i^2 v_{v,i}) \right)_{\Lambda_i} + \sum_i \left[\overline{p}_{v,i} \pi R_i^2 v_{v,i}|_{s=L} - \overline{p}_{v,i} \pi R_i^2 v_{v,i}|_{s=0} \right].$$

Using the continuity of the pressure at junction points, the last term in the previous expression can be arranged junction by junction as follows,

$$\sum_i \left[\overline{p}_{v,i} \pi R_i^2 v_{v,i}|_{s=L} - \overline{p}_{v,i} \pi R_i^2 v_{v,i}|_{s=0} \right]$$

$$= \sum_j \overline{p}_v|_{\boldsymbol{y}_j} \left[\sum_{i \in \mathcal{K}_j^+} \pi R_i^2 v_{v,i}|_{\boldsymbol{y}_j} - \sum_{i \in \mathcal{K}_j^-} \pi R_i^2 v_{v,i}|_{\boldsymbol{y}_j} \right] + \sum_{i \in \mathcal{E}} \overline{p}_v \pi R_i^2 v_v|_{\boldsymbol{z}_i} + \sum_{i \in \mathcal{B}} \left[\overline{p}_v \pi R_i^2 v_v|_{\boldsymbol{x}_i^+} - \overline{p}_v \pi R_i^2 v_v|_{\boldsymbol{x}_i^-} \right].$$

We finally use the last term of the previous expression to enforce pressure boundary conditions at the boundary points of the network, namely $\overline{p}_v|_{\boldsymbol{x}_i^+} = g_v^+$ and $\overline{p}_v|_{\boldsymbol{x}_i^-} = g_v^-$ for any $i \in \mathcal{B}$. Combining all these equations, the weak formulation of problem (8) reads as follows:

$$
\begin{cases}
\left(\nabla \cdot \mathbf{u}_t, q_t \right)_\Omega - \left(2\pi R f(\overline{\overline{p}}_t, \overline{p}_v) \delta_\Lambda, q_t \right)_\Omega = 0 & \forall q_t \in Q_t, \\[2mm]
\frac{\mu_t}{K} \left(\mathbf{u}_t, \boldsymbol{v}_t \right)_\Omega - \left(p_t, \nabla \cdot \boldsymbol{v}_t \right)_\Omega = -\left(g_t, \boldsymbol{v}_t \cdot \boldsymbol{n}_t \right)_{\partial\Omega} & \forall \boldsymbol{v}_t \in \boldsymbol{V}_t, \\[2mm]
\sum_i \left(\partial_s(\pi R_i^2 \overline{u}_{v,i}), q_v \right)_{\Lambda_i} + \sum_i \left(2\pi R f(\overline{\overline{p}}_t, \overline{p}_v), q_v \right)_{\Lambda_i} - \sum_{i \in \mathcal{E}} q_v \pi R_i^2 \overline{u}_{v,i}|_{\boldsymbol{z}_i} \\[1mm]
\qquad - \sum_j q_v|_{\boldsymbol{y}_j} \left[\sum_{i \in \mathcal{K}_j^+} \pi R_i^2 \overline{u}_{v,i}|_{\boldsymbol{y}_j} - \sum_{i \in \mathcal{K}_j^-} \pi R_i^2 \overline{u}_{v,i}|_{\boldsymbol{y}_j} \right] = 0 & \forall q_v \in Q_v, \\[2mm]
\sum_i \left(-2\frac{\mu_{v,i}}{R_i^2} \phi'(1)\left(1 + \kappa_i^2 R_i^2\right) \pi R_i^2 \overline{u}_{v,i}, v_{v,i} \right)_{\Lambda_i} - \sum_i \left(\overline{p}_v, \partial_s(\pi R_i^2 v_{v,i}) \right)_{\Lambda_i} \\[1mm]
\qquad + \sum_j \overline{p}_v|_{\boldsymbol{y}_j} \left[\sum_{i \in \mathcal{K}_j^+} \pi R_i^2 v_{v,i}|_{\boldsymbol{y}_j} - \sum_{i \in \mathcal{K}_j^-} \pi R_i^2 v_{v,i}|_{\boldsymbol{y}_j} \right] + \sum_{i \in \mathcal{E}} \overline{p}_v \pi R_i^2 v_v|_{\boldsymbol{z}_i} \\[1mm]
\qquad = -\sum_{i \in \mathcal{B}} \left[g_v^+ \pi R_i^2 v_v|_{\boldsymbol{x}_i^+} - g_v^- \pi R_i^2 v_v|_{\boldsymbol{x}_i^-} \right] & \forall v_v \in V_v.
\end{cases}
$$
$$(15)$$

For the hematocrit, we multiply the governing equation (14) by a test function $w_i \in H^1(\Lambda_i)$. Then, we use Green's formula to transfer the derivative from H_i to w_i and we sum over the branches. In this way we obtain the following expression,

$$\sum_i \left(\partial_s(\pi R_i^2 \overline{u}_{v,i} H_i), w_i \right)_{\Lambda_i} = -\sum_i \left(\pi R_i^2 \overline{u}_{v,i} H_i, \partial_s w_i \right)_{\Lambda_i} + \sum_i \left[\pi R_i^2 \overline{u}_{v,i} H_i w_i|_{s=L} - \pi R_i^2 \overline{u}_{v,i} H_i w_i|_{s=0} \right].$$

Then, we rearrange the last term of the previous equation junction by junction, as well as we isolate the terms on the boundary and on the dead ends,

$$+ \sum_i \left[\pi R_i^2 \overline{u}_{v,i} H_i w_i |_{s=L} - \pi R_i^2 \overline{u}_{v,i} H_i w_i |_{s=0} \right] = \sum_j \left[\sum_{i \in \mathcal{K}_j^{out}} \pi R_i^2 \overline{u}_{v,i} H_i w_i |_{\boldsymbol{y}_j} - \sum_{i \in \mathcal{K}_j^{in}} \pi R_i^2 \overline{u}_{v,i} H_i w_i |_{\boldsymbol{y}_j} \right]$$

$$+ \sum_{i \in \mathcal{B}} \left[\pi R_i^2 \overline{u}_{v,i} H_i w_i |_{\boldsymbol{x}_i^{out}} - \pi R_i^2 \overline{u}_{v,i} H_i w_i |_{\boldsymbol{x}_i^{in}} \right] + \sum_{i \in \mathcal{E}} \pi R_i^2 \overline{u}_{v,i} H_i w_i |_{\boldsymbol{z}_i} \quad (16)$$

Using the previous expression, we enforce the mass balance of hematocrit at the network junctions and the boundary conditions. For this purpose we define the following quantities for the j-th junction. The blood flow split relative to all the inflow branches is,

$$F_{QB,j,i} = \frac{\pi R_i^2 \overline{u}_{v,i} |_{\boldsymbol{y}_j}}{\sum_{i \in \mathcal{K}_j^{out}} \pi R_i^2 \overline{u}_{v,i} |_{\boldsymbol{y}_j}} , \quad \forall i \in \mathcal{K}_j^{in} ,$$

and let $F_{QE,j,i}$ be the corresponding split of hematocrit,

$$\begin{cases} F_{QE,j,i} = 1 & if \operatorname{card}(\mathcal{K}_j^{in}) = 1; \\[2mm] F_{QE,j,i} = 0 & if \operatorname{card}(\mathcal{K}_j^{in}) = 2 \wedge F_{QB,j,i} \leq X_0; \\[2mm] \operatorname{logit}(F_{QE,j,i}) = A + B \operatorname{logit}(\frac{F_{QB,j,i} - X_0}{1 - 2X_0}) & if \operatorname{card}(\mathcal{K}_j^{in}) = 2 \wedge X_0 < F_{QB,j,i} < 1 - X_0; \\[2mm] F_{QE,j,i} = 1 & if \operatorname{card}(\mathcal{K}_j^{in}) = 2 \wedge F_{QB,j,i} \geq 1 - X_0. \end{cases}$$

$$(17)$$

As a consequence of these definitions, the discharge hematocrit entering each branch downstream the j-th junction is,

$$\pi R_i^2 \overline{u}_{v,i} H_i |_{\boldsymbol{y}_j} = F_{QE,j,i} \sum_{i \in \mathcal{K}_j^{out}} \pi R_i^2 \overline{u}_{v,i} H_i |_{\boldsymbol{y}_j} .$$

We weakly enforce the hematocrit split conditions in the variational formulation as follows,

$$\sum_{i \in \mathcal{K}_j^{in}} \pi R_i^2 \overline{u}_{v,i} H_i w_i |_{\boldsymbol{y}_j} = \sum_{i \in \mathcal{K}_j^{in}} F_{QE,j,i} w_i |_{\boldsymbol{y}_j} \left(\sum_{i \in \mathcal{K}_j^{out}} \pi R_i^2 \overline{u}_{v,i} H_i |_{\boldsymbol{y}_j} \right) .$$

We also enforce the boundary conditions for hematocrit at the boundary of the network,

$$\pi R_i^2 \overline{u}_{v,i} H_i w_i |_{\boldsymbol{x}_i^{in}} = \pi R_i^2 \overline{u}_{v,i} H_0 w_i |_{\boldsymbol{x}_i^{in}} .$$

Substituting, for clarity, these terms into (16), we obtain,

$$+ \sum_i \left[\pi R_i^2 \overline{u}_{v,i} H_i w_i|_{s=L} - \pi R_i^2 \overline{u}_{v,i} H_i w_i|_{s=0} \right]$$

$$= \sum_j \sum_{i \in \mathcal{K}^{out}} \pi R_i^2 \overline{u}_{v,i} H_i w_i|_{\boldsymbol{y}_j} + \sum_{i \in \mathcal{B}} \pi R_i^2 \overline{u}_{v,i} H_i w_i|_{\boldsymbol{x}_i^{out}} + \sum_{i \in \mathcal{E}} \pi R_i^2 \overline{u}_{v,i} H_i w_i|_{\boldsymbol{z}_i}$$

$$- \sum_j \sum_{i \in \mathcal{K}_j^{in}} F_{QE,j,i} w_i|_{\boldsymbol{y}_j} \left(\sum_{i \in \mathcal{K}_j^{out}} \pi R_i^2 \overline{u}_{v,i} H_i|_{\boldsymbol{y}_j} \right) - \sum_j \sum_{i \in \mathcal{B}} \pi R_i^2 \overline{u}_{v,i} H_0 w_i|_{\boldsymbol{x}_i^{in}} \, .$$

Consequently, the variational formulation of the hematocrit governing equation reads as follows,

$$- \sum_i \left(\pi R_i^2 \overline{u}_{v,i} H_i \, , \, \partial_s w_i \right)_{\Lambda_i}$$

$$+ \sum_j \sum_{i \in \mathcal{K}^{out}} \pi R_i^2 \overline{u}_{v,i} H_i w_i|_{\boldsymbol{y}_j} + \sum_{i \in \mathcal{B}} \pi R_i^2 \overline{u}_{v,i} H_i w_i|_{\boldsymbol{x}_i^{out}} + \sum_{i \in \mathcal{E}} \pi R_i^2 \overline{u}_{v,i} H_i w_i|_{\boldsymbol{z}_i}$$

$$- \sum_j \sum_{i \in \mathcal{K}_j^{in}} F_{QE,j,i} w_i|_{\boldsymbol{y}_j} \left(\sum_{i \in \mathcal{K}_j^{out}} \pi R_i^2 \overline{u}_{v,i} H_i|_{\boldsymbol{y}_j} \right) = \sum_j \sum_{i \in \mathcal{B}} \pi R_i^2 \overline{u}_{v,i} H_0 w_i|_{\boldsymbol{x}_i^{in}} \quad \forall w_i \in H^1(\Lambda_i) \, .$$

$$(18)$$

3.2. Numerical approximation and solution strategy

3.2.1. Finite element approximation The discretization of problem (15) is achieved by means of the finite element method. One of the main advantages of our formulation is that the partitions of Ω and Λ are completely independent. For this reason we address the two approximations separately.

We denote with $\mathcal{T}_t^h$ an admissible family of partitions of $\bar{\Omega}$ into tetrahedrons K

$$\bar{\Omega} = \bigcup_{K \in \mathcal{T}_t^h} K,$$

that satisfies the usual conditions of a conforming triangulation of Ω. Here, h denotes the mesh characteristic size, i.e. $h = \max_{K \in \mathcal{T}_t^h} k_K$, being h_K the diameter of simplex K. Moreover, we are implicitly assuming that Ω is a *polygonal* domain. The solutions of (15) are approximated using discontinuous piecewise-polynomial finite elements for pressure and $\boldsymbol{H}_{div}$-conforming *Raviart-Thomas* finite elements [2] for velocity, namely

$$Y_k^h := \{v_h \in L^2(\Omega), \ v_h|_K \in P_k(K) \quad \forall K \in \mathcal{T}_t^h\},$$

$$\boldsymbol{RT}_k^h := \{\mathbf{w}_h \in \boldsymbol{H}_{div}(\Omega), \ \mathbf{w}_h|_K \in P_k(K; \mathbb{R}^d) \oplus \mathbf{x}\, P_k(K) \quad \forall K \in \mathcal{T}_t^h\},$$

for every integer $k \geq 0$, where $\mathcal{P}_k$ indicates the standard space of polynomials of degree $\leq k$ in the variables $\mathbf{x} = (x_1, \ldots, x_d)$. For the simulations presented later on, the lowest order *Raviart-Thomas* approximation has been adopted, corresponding to $k = 0$ above.

Concerning the capillary network, we adopt the same approach used at the continuous level, namely we split the network branches in separate sub-domains. Furthermore, each curved branch Λ_i is approximated by a piecewise linear 1D line, denoted with Λ_i^h. More precisely the latter is a partition of the i-th network branch made by a sufficiently large number of segments, named $S \subset \Lambda_i^h$. In this way, we obtain the following discrete domain:

$$\Lambda^h = \bigcup_{i=1}^{N} \Lambda_i^h \, .$$

The solution of (15) over a given branch Λ_i^h is approximated using continuous piecewise-polynomial finite element spaces for both pressure and velocity. Since we want the vessel velocity to be discontinuous at multiple junctions, we define the related finite element space over the whole network as the collection of the local spaces of the single branches. Conversely the pressure has been assumed to be continuous over the network, therefore its finite element approximation is standard. We will use the following families of finite element spaces for pressure and velocity, respectively:

$$X_{k+1}^h (\Lambda) := \{w_h \in C^0(\bar{\Lambda}), \, w_h|_S \in P_{k+1}(S) \quad \forall S \in \Lambda^h\},$$
$$W_{k+2}^h (\Lambda) := \bigcup_{i=1}^{N} X_{k+2}^h \left(\Lambda_i^h \right),$$

for every integer $k \geq 0$. As a result, we use generalized Taylor-Hood elements on each network branch, satisfying in this way the local stability of the mixed finite element pair for the network. At the same time, we guarantee that the pressure approximation is continuous over the entire network Λ^h. In particular, for the numerical experiments shown later on we have used the lowest order, that is $k = 0$.

For hematocrit we proceed as for the velocity approximation. In particular, we approximate equation (18) with the finite element space W_{k+2}^h defined on Λ_i^h. For the sake of generality, let us define the families of discrete subspaces of the functional spaces for $k \geq 0$:

$$\boldsymbol{V}_t^h = \boldsymbol{RT}_k^h(\Omega) \quad \text{and} \quad Q_t^h = Y_k^h(\Omega) \, ,$$
$$V_v^h = W_{k+2}^h(\Lambda^h) \quad \text{and} \quad Q_v^h = X_{k+1}^h(\Lambda^h) \quad \text{and} \quad W_v^h = W_{k+2}^h(\Lambda^h) \, .$$

Then, the finite element approximation of equations (15) and (18) reads as follows: find $\boldsymbol{u}_t^h \in$ $\boldsymbol{V}_t^h$, $p_t^h \in Q_t^h$, $u_v^h \in V_v^h$, $p_v^h \in Q_v^h$, $H^h \in W_v^h$ such that

$$
\begin{cases}
\left(\nabla \cdot \boldsymbol{u}_t^h, q_t^h\right)_\Omega - \left(2\pi R f(\overline{p}_t^h, \overline{p}_v^h)\delta_\Lambda, q_t^h\right)_\Omega = 0 & \forall q_t^h \in Q_t^h, \\[2mm]
\frac{\mu_t}{K}\left(\boldsymbol{u}_t^h, \boldsymbol{v}_t^h\right)_\Omega - \left(p_t, \nabla \cdot \boldsymbol{v}_t^h\right)_\Omega = -\left(g_t, \boldsymbol{v}_t^h \cdot \boldsymbol{n}_t\right)_{\partial\Omega} & \forall \boldsymbol{v}_t^h \in \boldsymbol{V}_t^h, \\[2mm]
\sum_i \left(\partial_s(\pi R_i^2 \overline{u}_{v,i}^h), q_v^h\right)_{\Lambda_i^h} + \sum_i \left(2\pi R f(\overline{p}_t^h, \overline{p}_v^h), q_v^h\right)_{\Lambda_i^h} - \sum_{i\in\mathcal{E}} q_v^h \pi R_i^2 \overline{u}_{v,i}^h|_{\boldsymbol{z}_i} & \\[1mm]
\quad - \sum_j q_v^h|_{\boldsymbol{y}_j}\left[\sum_{i\in\mathcal{K}_j^+} \pi R_i^2 \overline{u}_{v,i}^h|_{\boldsymbol{y}_j} - \sum_{i\in\mathcal{K}_j^-} \pi R_i^2 \overline{u}_{v,i}^h|_{\boldsymbol{y}_j}\right] = 0 & \forall q_v^h \in Q_v^h, \\[2mm]
\sum_i \left(-2\frac{\mu_{v,i}}{R_i^2}\phi'(1)\left(1+\kappa_i^2 R_i^2\right)\pi R_i^2 \overline{u}_{v,i}^h, v_{v,i}^h\right)_{\Lambda_i} - \sum_i \left(\overline{p}_v^h, \partial_s(\pi R_i^2 v_{v,i}^h)\right)_{\Lambda_i^h} & \\[1mm]
\quad + \sum_j \overline{p}_v^h|_{\boldsymbol{y}_j}\left[\sum_{i\in\mathcal{K}_j^+} \pi R_i^2 v_{v,i}^h|_{\boldsymbol{y}_j} - \sum_{i\in\mathcal{K}_j^-} \pi R_i^2 v_{v,i}^h|_{\boldsymbol{y}_j}\right] + \sum_{i\in\mathcal{E}} \overline{p}_v^h \pi R_i^2 v_v^h|_{\boldsymbol{z}_i} & \\[1mm]
\quad = -\sum_{i\in\mathcal{B}}\left[g_v^+ \pi R_i^2 v_v^h|_{\boldsymbol{x}_i^+} - g_v^- \pi R_i^2 v_v^h|_{\boldsymbol{x}_i^-}\right] & \forall v_v^h \in V_v^h, \\[2mm]
-\sum_i \left(\pi R_i^2 \overline{u}_{v,i}^h H_i^h, \partial_s w_i^h\right)_{\Lambda_i^h} & \\[1mm]
\quad + \sum_j \sum_{i\in\mathcal{K}^{out}} \pi R_i^2 \overline{u}_{v,i}^h H_i^h w_i^h|_{\boldsymbol{y}_j} + \sum_{i\in\mathcal{B}} \pi R_i^2 \overline{u}_{v,i}^h H_i^h w_i^h|_{\boldsymbol{x}_i^{out}} + \sum_{i\in\mathcal{E}} \pi R_i^2 \overline{u}_{v,i}^h H_i^h w_i^h|_{\boldsymbol{z}_i} & \\[1mm]
\quad - \sum_j \sum_{i\in\mathcal{K}_j^{in}} F_{QE,j,i} w_i^h|_{\boldsymbol{y}_j}\left(\sum_{i\in\mathcal{K}_j^{out}} \pi R_i^2 \overline{u}_{v,i}^h H_i^h|_{\boldsymbol{y}_j}\right) = \sum_j \sum_{i\in\mathcal{B}} \pi R_i^2 \overline{u}_{v,i}^h H_0 w_i^h|_{\boldsymbol{x}_i^{in}} & \forall w_i^h \in W_v^h.
\end{cases}
$$
$$\tag{19}$$

The global error of the numerical solution is affected by multiple factors: (i) the approximation properties of the scheme (19) with respect to the exact equations (15) and (18); (ii) the interpolation properties of the finite element spaces chosen to represent the unknowns, namely velocity, pressure and hematocrit; (iii) the approximation of the morphology of the curved network branches by means of piecewise linear segments with nodes located on the exact geometry. Since the discrete problem is strongly consistent with the exact equations, and all the integral forms are computed exactly when applied to the discrete functions, we conclude that the contribution (i) is null. For the finite element spaces, we will use the lowest order formulation defined above, that is $k = 0$. This choice entails *linear* convergence with respect to the mesh characteristic size, for velocity and pressure in Ω and *quadratic* convergence for velocity and pressure in Λ. Finally, it can be shown that the third type of approximation, namely the difference between the network Λ with Λ^h, introduces an error that scales *quadratically* with the characteristic size of the mesh defined on Λ^h. For the simulations presented in the next section we have derived the analytical solution of the problem on a single, curved but impermeable capillary, and we have compared it with the numerical solution for different mesh sizes, see Figure 3 panel C. Even though the data are not explicitly reported, the quadratic convergence rate for the velocity is confirmed.

We notice that problem (19) is a fully coupled nonlinear problem. Indeed, velocities and pressures on Ω and Λ are coupled through the linear term $f(\overline{p}_t, \overline{p}_v)$, while the velocity field on Λ is affected

by hematocrit through the nonlinear viscosity model. More precisely we have $\mu_{v,i} = \mu_{v,i}(H_i)$ as prescribed in equation (9). Finally, hematocrit is heavily affected by the flow field in the network, through transport and also by the flow split at network branches, defined in (17). In order to solve the problem, we will adopt an iterative splitting strategy, addressed in the next section.

3.2.2. Iterative strategy for the solution of the nonlinear problem To describe the iterative splitting strategy used to decouple (19) we define a shorthand notation. More precisely, let us group the first four equations of (19) into the *fluid mechanics* operator $\mathcal{F}^h$. Given Ω, Λ^h, the external data g_t, g_v and the parameters for the porous medium K, μ_t the operator $\mathcal{F}^h$ takes as input the viscosity of the fluid μ_v as a function defined on Λ^h and gives back the solution of the fluid mechanics problem, namely $[\boldsymbol{u}_t^h, u_v^h, p_t^h, p_v^h] = \mathcal{F}^h(\mu_v)$. In algebraic terms is a large system of linear and nonlinear equations, presented in the appendix A, see in particular (25). Similarly, the last equation of (19) can be represented as the operator $\mathcal{H}^h$, such that given the velocity field in the network u_v^h it gives back the hematocrit level at each point of Λ^h, precisely $H^h = \mathcal{H}^h(u_v^h)$. This is a large system of linear equations defined in (26). Using these operators the iterative method to solve (19) consists of performing the following steps for any $k > 0$ until convergence:

0. we initialize the fluid mechanics problem by calculating all the matrices of (25) that are independent of μ_v, namely all except from $\mathbb{M}_{vv}$. We calculate $\mathbb{M}_{vv}$ using a uniform initial guess of the apparent blood viscosity $\mu_v^0 = \mu_{ref}$ defined in (12).

1. (if $k > 0$ we build the matrix $\mathbb{M}_{vv}(\mu_v^{k-1})$ and we solve the fluid mechanics problem

$$
\begin{bmatrix}
\mathbb{M}_{tt} & -\mathbb{D}_{tt}^T & \mathbb{O} & \mathbb{O} \\
\mathbb{D}_{tt} & \mathbb{B}_{tt} & \mathbb{O} & -\mathbb{B}_{tv} \\
\mathbb{O} & \mathbb{O} & \mathbb{M}_{vv}(\mu_v^{k-1}) & -\mathbb{D}_{vv}^T - \mathbb{J}_{vv}^T \\
\mathbb{O} & -\mathbb{B}_{vt} & \mathbb{D}_{vv} + \mathbb{J}_{vv} & \mathbb{B}_{vv}
\end{bmatrix}
\begin{bmatrix}
\mathbf{U}_t^* \\
\mathbf{P}_t^* \\
\mathbf{U}_v^* \\
\mathbf{P}_v^*
\end{bmatrix}
=
\begin{bmatrix}
\mathbf{F}_t \\
-\mathbb{B}_{tt}\delta\pi \\
\mathbf{F}_v \\
\mathbb{B}_{vv}\delta\pi
\end{bmatrix}
$$

to determine $[\boldsymbol{u}_t^{h,*}, u_v^{h,*}, p_t^{h,*}, p_v^{h,*}]$ from the vectors $\mathbf{U}_t^*, \mathbf{P}_t^*, \mathbf{U}_v^*, \mathbf{P}_v^*$ using expressions (22), (23), where $*$ denotes an auxiliary solution to be used in the next step;

2. we apply the relaxation of the velocity and pressure fields to enhance convergence, namely for a given $\alpha \in (0, 1]$ we calculate

$$\boldsymbol{u}_t^{h,k} = \alpha\boldsymbol{u}_t^{h,*} + (1-\alpha)\boldsymbol{u}_t^{h,k-1}, \qquad u_v^{h,k} = \alpha u_v^{h,*} + (1-\alpha)u_v^{h,k-1};$$

$$p_t^{h,k} = \alpha p_t^{h,*} + (1-\alpha)p_t^{h,k-1}, \qquad p_v^{h,k} = \alpha p_v^{h,*} + (1-\alpha)p_v^{h,k-1};$$

3. we build the matrices defined in (26), using the velocity field in the network calculated at the previous step, namely $\boldsymbol{u}_v^{h,k}$. Then, we solve the hematocrit problem

$$\left[\mathbb{B}_h(u_v^{h,k}) + \mathbb{J}_h(u_v^{h,k}) + \mathbb{O}_h(u_v^{h,k})\right]\left[\mathbf{H}^*\right] = \left[\mathbf{F}_h\right]$$

to determine $H^{h,*}$ from the vector $\mathbf{H}^*$ using expression (24);

4. we apply the relaxation $H^{h,k} = \beta H^{h,*} + (1-\beta)H^{h,k-1}$ with $\beta \in (0,1]$;

5. we update the apparent viscosity of blood, $\mu_{v,i}^k = \mu_{v,i}(H_i^{h,k})$ for $i = 1,\ldots,N$ using the formula (9).

6. given fixed tolerances $\epsilon_\mathcal{F}$, $\epsilon_\mathcal{H}$, we test the convergence by means of the following indicators,

$$\frac{\left\|\mathbf{U}_v^{k+1} - \mathbf{U}_v^k\right\|}{\left\|\mathbf{U}_v^k\right\|} + \frac{\left\|\mathbf{P}_v^{k+1} - \mathbf{P}_v^k\right\|}{\left\|\mathbf{P}_v^k\right\|} + \frac{\left\|\mathbf{U}_t^{k+1} - \mathbf{U}_t^k\right\|}{\left\|\mathbf{U}_t^k\right\|} + \frac{\left\|\mathbf{P}_t^{k+1} - \mathbf{P}_t^k\right\|}{\left\|\mathbf{P}_t^k\right\|} < \epsilon_\mathcal{F},$$

$$\frac{\left\|\mathbf{H}^{k+1} - \mathbf{H}^k\right\|}{\left\|\mathbf{H}^k\right\|} < \epsilon_\mathcal{H}$$

If the test is satisfied, then we stop the iterations. Otherwise, we go back to point 1.

4. NUMERICAL SIMULATIONS

In this section we apply the computational model for blood flow and hematocrit transport to various test cases of increasing complexity. The simplest ones, more precisely a single capillary branch and a bifurcation, are presented to validate the predictions of the model against analytical solutions and expected behaviors. In this case, we also elucidate the sensitivity of the outcome with respect to some parameters of the model, such as the curvature of the capillaries and their permeability. Later on we present a more complex, but still idealized, model for a capillary network. In this case, we investigate the ability of the model to capture the macroscopic traits of microcirculation.

4.1. Single capillary branch case

We present simulations of blood flow in a single branch of capillary vessel, interacting with the surrounding tissue, modeled as a homogeneous porous medium. For this idealized experiment we consider a tissue sample represented by a cube of side D. A single capillary branch crosses the tissue sample from side to side. Different capillary shapes are considered, namely we simulate a straight segment, a circular arc with intermediate curvature (such that the dimensionless parameter

symbol	Parameter	Unit	Value	Ref.
d	characteristic length	m	1×10^{-4}	[40]
D	characteristic length of the domain	m	1×10^{-4}	[40]
R	average radius	m	4×10^{-6}	[65]
K	tissue hydraulic conductivity	m^2	1×10^{-18}	[7]
μ_t	interstitial fluid viscosity	cP	1.2	[60]
μ_v	blood viscosity	cP	Pries formula	[50]
L_p	wall hydraulic conductivity	$\mathrm{m^2\,s\,kg^{-1}}$	10^{-12}	[7]
P	characteristic pressure	Pa	133.32	[7]
U	characteristic velocity	$\mathrm{m\,s^{-1}}$	1×10^{-3}	[49]
$\delta\pi$	oncotic pressure gradient	$mmHg$	25	[59]
σ	reflection coefficient	$[-]$	0.95	[36]

Table I. Physiological parameters used for all the numerical tests (unless differently specified).

κR is equal to 0.06) and a circular arc with high curvature (such that $\kappa R = 0.11$, shown in Figure 3). When the curvature changes, the dimension of the domain is adjusted such that in all cases the length of the channel, L, is constant and equal to D. The velocity profile for a curved pipe with $\kappa R = 0.11$ is visualized in Figure 1. We observe it looses symmetry with respect to the axis of the channel. The parameters of the model adopted in the simulations are collected (with description, units and sources) in Table I.

Concerning the boundary conditions, we apply the pressure at the endpoints of the network, the hematocrit at the corresponding inflow points and we allow for fluid exchange at the artificial interfaces that separate the tissue sample with the exterior. The latter effect is described by a condition of type

$$\boldsymbol{u}_t \cdot \boldsymbol{n}_t = \beta_t(p_t - p_0),$$

where β_t is the boundary conductivity of the tissue matrix and p_0 denotes a far field pressure. The data and parameters used for boundary conditions are reported in Table II. In particular, the value of the pressure drop is determined on the basis of a prescribed value of the blood flow velocity in small capillaries. Assuming $u_v \simeq 1\,mm/s$, the blood flow rate through a capillary with $R = 4\,\mu m$ is

$$Q_b = \pi R^2 u_v = 5.03 \times 10^{-14}\,m^3/s. \tag{20}$$

Using (20), $\mu_v \simeq 9.33\,cP$ form [50] and Poiseuille's law, with the hypothesis of no transcapillary flow, the pressure drop between the inlet and the outlet of the capillary will be equal to,

$$\delta p_v = Q_b \frac{8\mu_v L}{\pi R^4} = 3.5\,mmHg.$$

Finally, we need to determine inlet and outlet pressures. This choice depends on the position of the capillary segment in the microvasculature. To this purpose, we define $\overline{p}_v^*$ as the value of $\overline{p}_v$ for which the net filtration pressure is zero (for an average tissue pressure equal to the far field pressure p_0): if $\overline{p}_v > \overline{p}_v^*$ there will be a net fluid filtration, while if $\overline{p}_v < \overline{p}_v^*$ there will be a net fluid absorption. Considering the parameters in Table I and a constant interstitial pressure $p_t \simeq p_0 = -1\,mmHg$, we obtain,

$$\overline{p}_v^* = p_0 + \sigma\delta\pi = -1 + 0.95 \cdot 25 = 22.75\,mmHg.$$

On the basis of the observation that the microvascular pressure ranges between 32 and 15 $mmHg$ (see [59]) this value, for a vessel near the arteriolar end of the capillary network, we set $p_{inlet} = 32\,mmHg$ and $p_{outlet} = 28.5\,mmHg$, such that both values are above $\overline{p}_v^*$. For a portion of capillary near the venular circulation we set $p_{inlet} = 18.5\,mmHg$ and $p_{outlet} = 15\,mmHg$. In the latter case we expect that the capillary will absorb fluid from the intestitium.

Symbol	B.C.s	Unit	Value	Ref.
δp	hydrostatic pressure drop	$mmHg$	3.5	[59]
p_0	far field pressure	$mmHg$	-1	[12]
β_t	boundary conductivity	$m^2 s/kg$	5×10^{-11}	[5]
H_0	hematocrit at inlet of capillary	$-$	0.45	[25]

Table II. Data and parameters for the boundary conditions in the capillary and tissue regions

In Figure 3 (panel C) we compare the computed and analytically determined values of the velocity magnitude. We observe that in such simple geometry and in case of impermeable capillary walls, the analytical solution is available for pressure, velocity and hematocrit variation along the axis of the capillary. For example, for a straight pipe the analytical solution for velocity and pressure is the Poiseuille's law. According to the 1D model equations, in the case of a pipe with curvature $\kappa > 0$ the analytical solution for the velocity is the following,

$$\overline{u}_v = -\frac{R^2}{8\mu_v(1 + \kappa^2 R^2)} \frac{\delta p}{L}.$$

In this case, the comparison of computed and analytical solutions is shown in Figure 3 (panel C). The hematocrit distribution can then be easily determined if an analytical formula for the
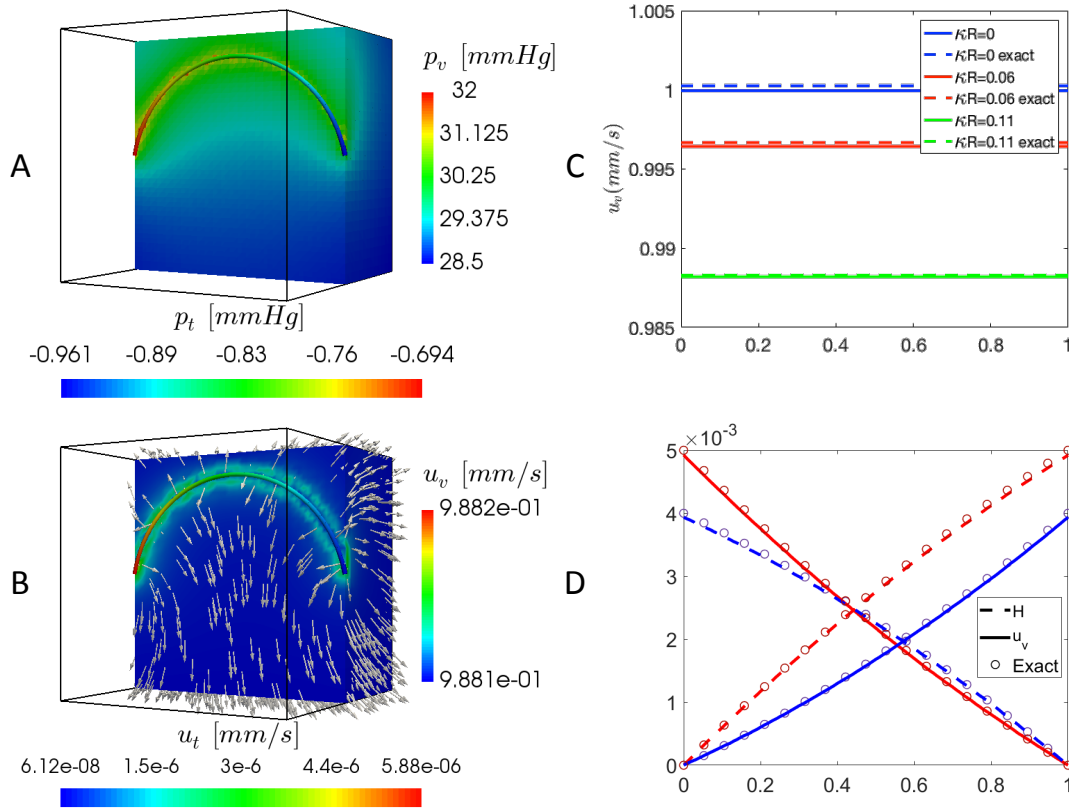
Figure 3. Panel A shows the geometrical configuration of the test case (highest curvature) with the variation of the pressure along the capillary and in the bulk. The inlet and outlet pressures are set to model the arteriolar side of the microvascular network ($p_{inlet} = 32\,mmHg$ and $p_{outlet} = 28.5\,mmHg$). Panel B compares the velocity profile (constant) and magnitude along the axis of the capillary and in the bulk, for the same test case as before. The velocity vectors of the interstitial velocity $\boldsymbol{u}_t$ are represented on a cross section of the tissue sample, on top of the contour plot of the velocity magnitude. Panels C and D show the evolution of variables along the axis of a capillary, being $s \in (0,1)$ the arc-length. Panel C shows the results for a impermeable capillary. For such case the analytical solution of the problem is available (dashed line) and it is compared with the numerical solution (continuous line), for different values of the curvature ($\kappa R = 0,\ 0.06,\ 0.11$). Panel D shows the % variation of the velocity magnitude (continuous line) and hematocrit (dashed line) along the capillary axis for the straight permeable capillary. Blue lines correspond to the venular end while red lines refer to the arteriolar side of the capillary network. The dots represent the analytical solution of problem (21) in terms of velocity and hematocrit variations.

velocity is known, because the hematocrit flow rate is constant along the pipe, namely $H(s)\overline{u}_v(s) = H_{inlet}\overline{u}_{v,inlet}$. Obviously, since the capillary is impermeable, the velocity profile is constant along the axis, but the velocity magnitude decreases with the curvature, because curved vessels oppose higher resistance to flow. We observe that this behavior is correctly captured by the model. The comparison of the numerical and analytical solution provides a verification of the numerical algorithm as well as a preliminary validation of the computational model. When we allow for plasma leakage from the capillary to the interstitial tissue, the flow and hematocrit axial distribution change in both regions, as shown on panels A and B of Figure 3. If we consider a capillary segment near the arteriolar side of the capillary network, due to overpressure in the capillary with respect to the interstitial volume, there is positive leakage and the capillary flow rate decreases accordingly. As a consequence of reduced plasma flow rate, the hematocrit slightly increases. These effects are

captured by model (8) that in this particular case simplifies to,

$$\frac{\partial^2 \bar{p}_v}{\partial s^2} - \frac{2\pi R L_p}{\pi R^4} 8\mu_v \left(1 + \kappa_i^2(s)R_i^2\right)\bar{p}_v(s) = -\frac{2\pi R L_p}{\pi R^4} 8\mu_v \left(1 + \kappa_i^2(s)R_i^2\right)[\bar{\bar{p}}_t + \sigma\delta\pi]\,, \qquad (21)$$

$$\bar{p}_v(s=0) = 32\,, \quad \bar{p}_v(s=1) = 28.5\,.$$

If the interstitial pressure is assumed to be constant, in this case equal to $\bar{\bar{p}}_t = -1mmHg$, the solution of the problem above can be determined analytically and it is

$$\bar{p}_v(s) = Ae^{-\sqrt{\frac{2\pi R L_p}{8\pi R^4}\mu_v(1+\kappa_i^2 R_i^2)}\,s} + Be^{\sqrt{\frac{2\pi R L_p}{8\pi R^4}\mu_v(1+\kappa_i^2 R_i^2)}\,s} + C\,,$$

with constants $\sqrt{\frac{2\pi R L_p}{8\pi R^4}\mu_v(1+\kappa_i^2 R_i^2)} = 0.0048296\, A = 366.984$ and $B = -357.734\, C = 22.75$ for a rectilinear single branch, $k = 0$. The velocity magnitude can be determined correspondingly, using equation $\bar{u}_v = -(R^2)/(8\mu_v(1+\kappa^2 R^2))\partial_s \bar{p}_v$ that gives $\bar{u}_v(s) = 0.506526e^{-0.0048296s} + 0.493758e^{0.0048296s}$. The variation of hematocrit is then equal to $H(s) = H_{inlet}\bar{u}_{v,inlet}/\bar{u}_v(s)$. The comparison of these analytical results with the computed ones is shown in Figure 3 (panel D) and it confirms the validity of the computational approach. Opposite trends are observed for a capillary segment closer to the venular end (see Panel D, blue lines, continuous line for velocity, dashed line for hematocrit). Although these effects are quantitatively small for a little portion of a capillary, they illustrate the ability of the computational model to accurately capture the interaction of plasma flow, interstitial filtration and hematocrit at the microscale.

4.2. Y-shaped bifurcations

This test case is useful to evaluate the accuracy of the computational model in the description of the Fahraeus-Lindqvist effect, that is the variation of apparent viscosity due to rearrangement of red blood cells in the flow, and the plasma skimming effect, that is the asymmetric distribution of hematocrit when channels downstream a bifurcation are different. These phenomena mostly depend on the geometrical configuration of the vascular network, while the permeability of the capillary walls weakly affects them. For this reason, we perform all the computational tests for bifurcations in the case of impermeable walls, namely we set $L_p = 0$. All the remaining parameters and boundary conditions are the ones of Tables I and II.

The geometrical model consists of a Y-shaped bifurcation, where all branches have the same length. The radii of the daughter branches are calculated on the basis of the Murray's law, that is $R_0^3 = R_1^3 + R_2^3$, where index (0) denotes the parent vessel and (1), (2) are the daughter channels. Unless differently specified, the daughter branches have equal radius, namely $R_1 = R_2$, which

	straight			curved $\kappa R = 0.06$			curved $\kappa R = 0.11$		
Branch	0	1	2	0	1	2	0	1	2
$\overline{u}_v$	0.6559	0.5222	0.5222	0.6542	0.5222	0.5194	0.6509	0.5222	0.5142
H	0.4500	0.4500	0.4500	0.4500	0.4508	0.4492	0.4500	0.4524	0.4475
$\pi R^2 H \overline{u}_v$	$1.48\,10^{-5}$	$7.42\,10^{-6}$	$7.42\,10^{-6}$	$1.48\,10^{-5}$	$7.43\,10^{-6}$	$7.37\,10^{-6}$	$1.47\,10^{-5}$	$7.46\,10^{-6}$	$7.26\,10^{-6}$
Balance	-6.34×10^{-13}			-2.92×10^{-13}			1.17×10^{-13}		

Table III. For the text cases of Figure 4 we report the values of velocity ($\overline{u}_v$), hematocrit (H) and hematocrit flow rate at the junction, for the parent (0) and the daughter channels (1-top side) and (2-bottom side). The residual of the hematicrit flux balance (value (0) = value (1) + value (2)) is reported at the bottom row.

allows us to determine $R_1 = R_2$ as a function of R_0 as in Table I. The current model is not sensitive to the angle of the daughter branches.

First, we analyze the role of curvature on the distribution of flow rate, hematocrit and viscosity downstream to a bifurcation. The results of simulations are collected in Figure 4. We notice that curvature increases the resistance to flow, which in turn affects the distribution of blood flow rate and hematocrit at the bifurcation. Differences with respect to the symmetric case are rather small, approximately of 1% for each quantity. However, we remind that we are considering a small portion of a normal capillary, namely the characteristic length is only $100\mu m$. For the more extended vasculature models, the difference will be amplified by the geometrical scale factor. Thanks to the fact that we consider impermeable capillary walls, we observe that mass balance at the bifurcation point is trivially verified by looking at flow rates and hematocrit flow rate at the endpoints of the network. As it appears from Table III, the balance of these quantities at the junctions of the network is satisfied within the tolerance of the numerical discretization.

As regards the viscosity, reported in the bottom row of Figure 4, we first verify that the predictions of the computational model are coherent with formula (9), also visualized in Figure 2. We observe that viscosity increases downstream to the bifurcation, even though the hematocrit sightly decreases in the bottom branch (because of increased resistance to flow). This is however in agreement with the model, because viscosity is highly sensitive to the variation of the capillary radius. Since this parameter decreases from 4 μm in the parent branch to 3.17 μm in the daughter branches, viscosity correspondingly increases (see Figure 2 for a visualization of this effect).

In Figure 5, we study the influence of the capillary radii (or diameters) of the daughter branches on the velocity, hematocrit and viscosity. More precisely, we increase the radius of the upper daughter branch of 5% and 10%, while we decrease the radius of the lower branch of the same amount. More precisely, Figure 5 gives a general overview of all the cases, while Figure 6 provides a more detailed analysis of the results for the 10% perturbation of the radius where the differences are more easily visible.

A quantitative analysis of these effects is reported in Table IV. From the analysis of flow rates we see that the $\pm 5\%$ and $\pm 10\%$ variation of the radius significantly affects the distribution of flow rate
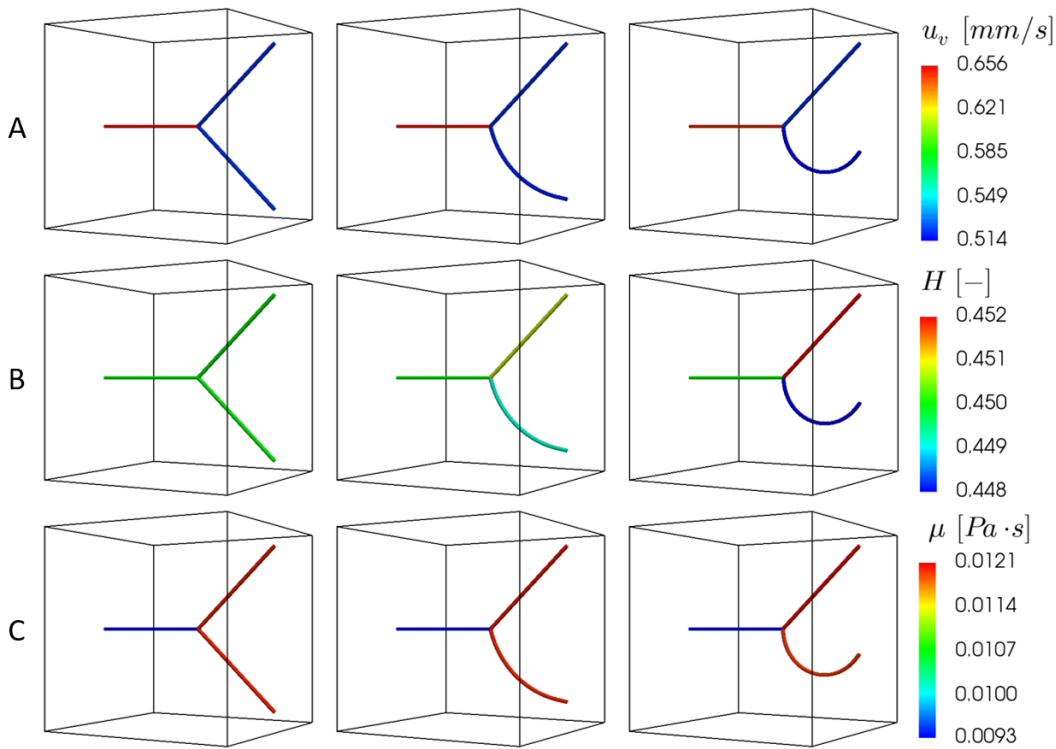
Figure 4. The top row (panel marked with A) shows the distribution of velocity in the bifurcation, for increasing levels of curvature $\kappa R = 0.0;\ 0.06;\ 0.11$, from left to right. We point out that all curved branches have the same length, such that the variation of resistance is only due to curvature. The middle row (marked with B) shows the hematocrit. In the bottom row (marked with C), we show the apparent viscosity, which is affected by the hematocrit and the capillary diameter according to (9), see also Figure 2.

downstream to the bifurcation, because resistance to flow is highly sensitive to the channel diameter at these small scales. Concerning hematocrit, we observe that its variations are also amplified with respect to the magnitude of the perturbation. More precisely, because of the plasma skimming effect, red blood cells hardly flow into the daughter branch with smaller radius. For this reason, hematocrit is lower in the branches where the radius has been decreased than in the ones where it was increased. The behavior of viscosity is less obvious, but still in line with the model. Indeed, we see that perturbations of the viscosity are damped with respect to those of the radius. This behavior can be interpreted using Figure 2, where we see that for small capillary radius, viscosity increases with hematocrit and decreases with capillary diameter. Our interpretation of Table IV is that these two effects partially compensate in the variation of viscosity.

This analysis confirms that blood velocity, hematocrit and viscosity are subject to a complex interaction at the bifurcation. More precisely, breaking the symmetry of the daughter vessel branches, generates significant variations on the blood flow rate, hematocrit and viscosity downstream to the bifurcation. The interaction between radius, flow rate, hematocrit and viscosity is highly nonlinear and hardly predictable with simple models that do not take into account their combined effects.
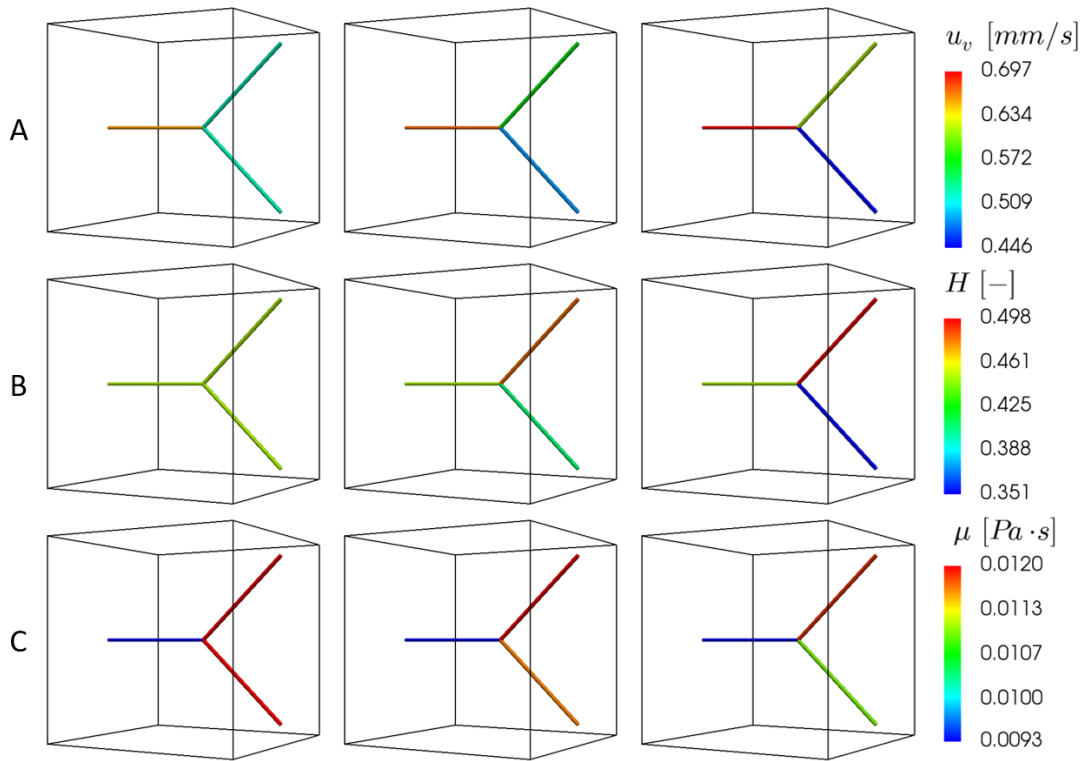
Figure 5. Velocities (panel A), hematocrit (penel B) and effective viscosity (panel C) are reported from top to bottom. In the first column, the daughter branches have equal radii $R_1 = R_2 = 3.17\mu m$. In the second column the radius of the upper branch is increased of 5% with respect to the nominal value while the one of the lower branch is decreased of the same amount. In the third column, the perturbation of the radii is $\pm 10\%$
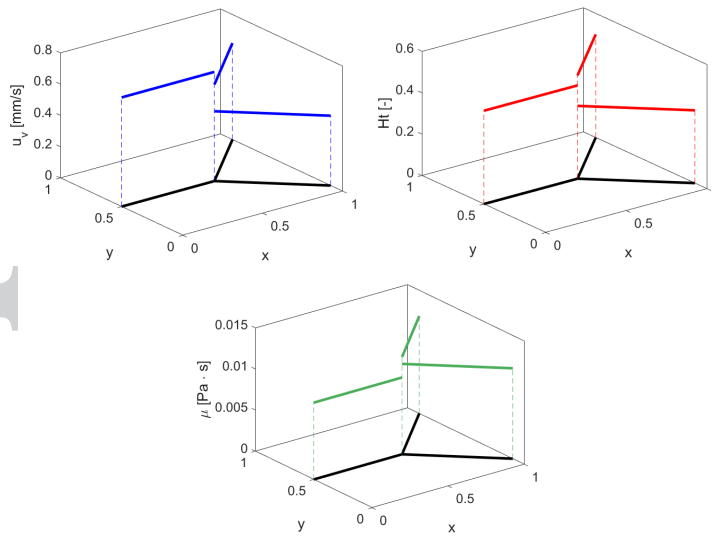

Figure 6. The linear variation along the axial coordinate s of velocity (blue), hematocrit (red) and effective viscosity (green) is shown from left to right for the particular case of $\pm 10\%$ radial perturbation downstream to the bifurcation.

4.3. Comparative studies on a microvascular network

In this section we use the computational model to simulate flow and hematocrit distribution in a fairly complex and realistic model of microvascular network. The section is subdivided in two parts.

	reference			5%			10%		
Branch	0	1	2	0	1	2	0	1	2
R	4.000	3.170	3.170	4.000	3.330	3.020	4.000	3.490	2.860
$\overline{u}_v$	0.656	0.522	0.522	0.669	0.568	0.483	0.697	0.617	0.446
$\%\overline{u}_v$				2%	9%	-8%	6%	18%	-15%
H	0.450	0.450	0.450	0.450	0.480	0.407	0.450	0.498	0.351
$\%H$				0%	7%	-10%	0%	11%	-22%
μ	0.009	0.012	0.012	0.009	0.012	0.012	0.009	0.012	0.011
$\%\mu$				0%	0%	-3%	0%	-2%	-8%

Table IV. Quantitative analysis of the simulations illustrated in Figure 5.

First we describe the procedure developed to generate artificial but realistic networks. Second we discuss the numerical simulations of flow and hematocrit transport obtained with the computational model.

4.3.1. A generator of artificial vascular networks The network that we use here satisfies the following criteria:

1. the morphology of the network respects the optimal distribution of a Voronoi tassellation;

2. the aspect ratio of each branch (L_i/R_i) is large enough to justify the one-dimensional flow assumption;

3. the radii of branches merging at any junction satisfy Murray's law;

4. the surface to volume density of the capillaries satisfies the physiologic value of $S/V = 7000$ m^{-1} [1];

The generation of such network is a complex (nonlinear) iterative procedure that is summarized below. We consider a representative cube of $D = 500$ μm side, because this is the typical length of a capillary vessel from the arteriolar to the venular ends. We notice that the characteristic size of the cube has increased 5 times with respect to the previous cases (where it was equal to 100 μm). As we will explain later, this change also influences the boundary conditions for the vasculature, spanning the entire pressure range of microvasculature from 32 to 15 $mmHg$.

The morphology of the network in such representative volume has been obtained by stacking several slabs containing a quasi-planar network. Following previous works [54, 55], each of these networks has been obtained using a biomimetic design principle based on the Voronoi tassellation model, which defines a partitioning of a plane into regions, based on the distance to seed points distributed on a subset of the plane. The edges of the Voronoi tassellation are equidistant to the seed points of the neighboring regions. Thanks to this property, the Voronoi partition may be considered to be a reasonable model for the distribution of capillaries, which should fill a biological tissue in a

way to maintain equal distance to the cells that populate it. The main parameter that influences the morphology of the network is then the number of seed points. We have screened several network configurations spanning from 5 to 15 seeds and we have decided to use networks arising from random distributions of 8 points on a 500 μm side square. This number of points is small enough to guarantee an aspect ratio of the channels that is sufficiently high (about $L_i/R_i = 4$), given an average radius of the branches of 4 μm. By randomly varying the distribution of 8 points, we have generated 100 different network configurations that satisfy the criterion on aspect ratio.

The second step consists of assigning to each branch a suitable radius that respects the Murray's law together with the additional physiological constraints of having a distribution of radii in the range $2 - 6$ μm with mean value, defined as $\sum_i R_i L_i / \sum_i L_i$, equal to 4 μm $\pm 5\%$. This task is achieved through the following procedure. We initialize the network with a uniform radius of 4 μm for every branch. Then we iterate among the following steps:

1. calculate the flow along the network, for suitable arteriolar and venular pressures. This step determines the connectivity of the network with respect of the flow and it allows us to identify bifurcations and anastomoses among all junctions. Finally, for any bifurcation, we randomly assign a split ratio a, defined below;

2. we apply the Murray's law:

$$\text{bifurcation} \quad R_{in,0}^3 = R_{out,1}^3 + R_{out,2}^3; \quad \text{for a given split ratio } a = \frac{R_{in,0}}{R_{out,1}}$$

$$\text{anastomosis} \quad R_{in,1}^3 + R_{in,2}^3 = R_{out,0}^3;$$

and we iterate until the connectivity of the network does not change from one step to the next. Since the split ratio at bifurcations is a random variable, this procedure is not deterministic and it gives out a different outcome at any run. This procedure was applied 100 times to each of the 100 networks morphologies obtained before. The procedure was also repeated with initial radii of 4, 4.5, 5 μm for a total of 3×10^4 possible configurations. Finally, we have discarded the ones with radii outside the interval $2 - 6$ μm and with a mean value of radius not equal to 4 μm $\pm 5\%$, ending up with about 10^4 valid configurations.

In this way, we have obtained a large population of planar networks that satisfy the first three criteria described above. The three-dimensional network configuration with a physiologic surface to volume density is obtained by stacking a suitable number of planar networks one above the other. After some preliminary calculations and numerical verifications, it is apparent that superposing 18 admissible planar networks on top of each other provides a surface to volume ratio of approximately 7000 m^{-1}, as desired. Every network can be randomly chosen among the database of $\simeq 10^4$
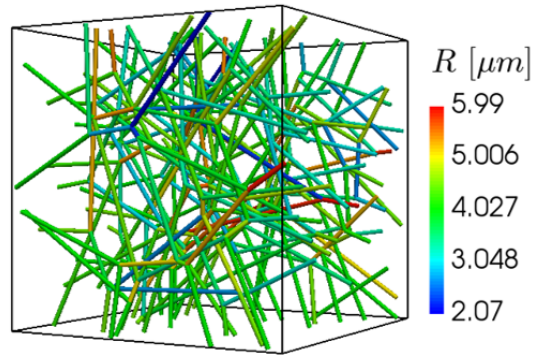
Figure 7. Visualization of the the morphology of the network and the distribution of the radii (μm).

configurations obtained by means of the previous procedure. To avoid perfect planarity, unlikely to be observed in reality, we have placed each network on the central plane of a slab that is $\Delta = 27.8$ μm thick. Then, we have perturbed the vertical coordinate of the network nodes of a random quantity less equal to $\Delta/2$.

This construction also facilitates the definition of boundary conditions on the network, because 2 of the 6 faces of the cube, precisely the ones parallel to the network planes, do not intersect the network branches. The remaining 4 faces (called lateral faces of the cube) are subdivided in two neighboring arteriolar faces and two neighboring venular ones. At the arteriolar endpoints of the network we set 32 $mmHg$ while at the venular ends we have 15 $mmHg$. The corresponding pressure drop drives the flow along the network.

In conclusion, this protocol allows for a great variability, but is controlled by a fairly small number of parameters that we have optimized in order to satisfy the physiological criteria listed above. One of these realistic configurations is the one used for the simulations discussed in the next section. In particular, we show in Figure 7 the morphology of the network (made of about 250 branches) and the distribution of the radius.

4.3.2. Calculation, visualization and analysis of blood flow and hematocrit in a realistic model of microvasculature The numerical simulations have been carried out using the finite element solver described in section 3.2. The geometrical model consists of 250 vascular branches with 20 elements on each branch, for a total of 5×10^3 nodes in the network. The interstitial volume is discretized with a uniform tetrahedral mesh obtained by distributing 41 nodes along each edge of the cube and consisting of approximately 4×10^5 tetrahedral elements.

The discrete model is transformed into a system of linear equations for the physical unknowns p_v, p_t, u_v, u_t, corresponding approximately to $5 \times 10^3, 4 \times 10^5, 10^4, 8 \times 10^5$ degrees of freedom, respectively. This is a fully coupled, block structured linear system that is solved by means of the
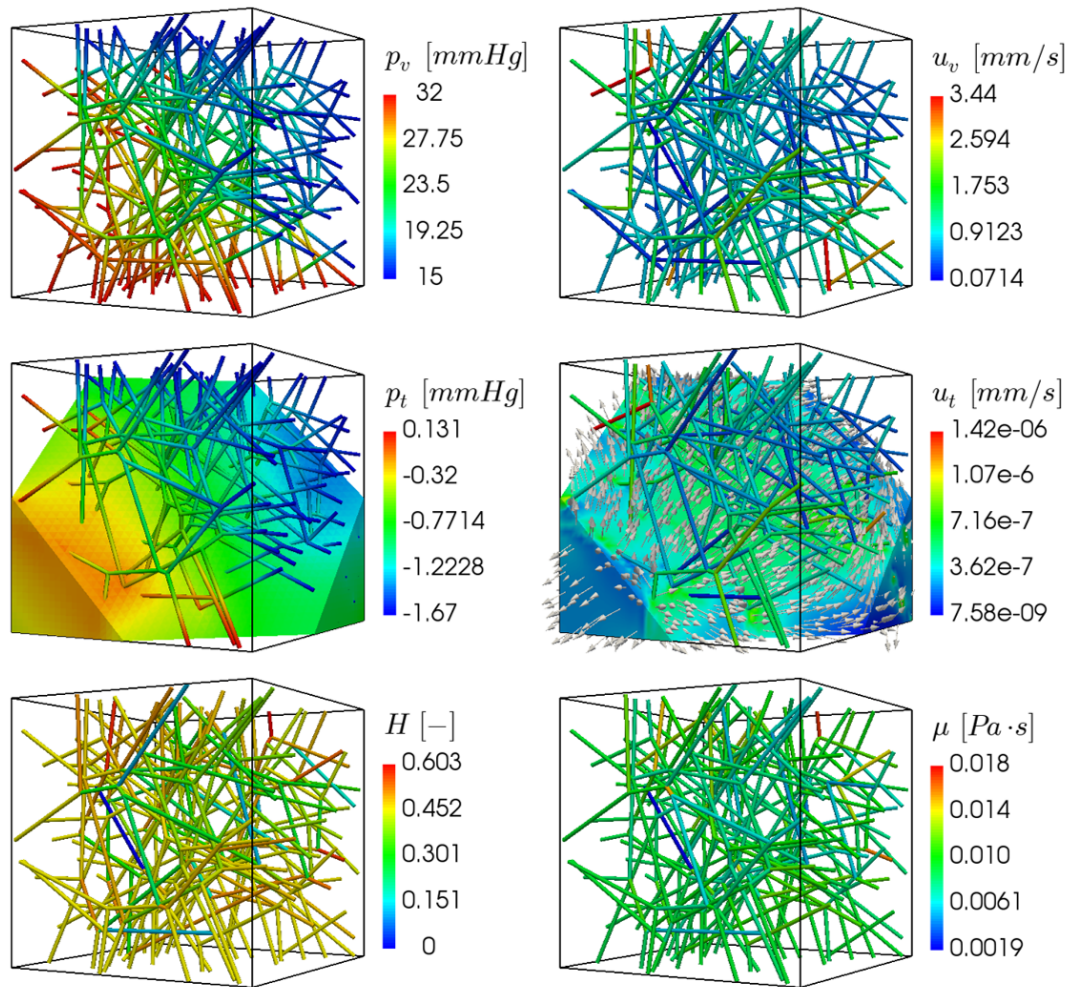
Figure 8. Visualization of the flow in a complex network interacting with the interstitial volume. In particular the panels show: the pressure drop along the network (top left); the velocity magnitude (top right); the pressure variation along a slice of the interstitial volume combined with the pressure in the network (middle left); the velocity field along a slice of the interstitial volume (the vectors show the direction and the colors the magnitude, middle right); the hematocrit distribution in the network (bottom left); and the effective viscosity (bottom right).

GMRES iterative solver, accelerated by a block preconditioner based on the Schur complements of the pressure problems. The solution of the system takes about 30 minutes on a standard desktop PC. However, this is not the total time necessary to perform the simulations shown below, because the Fahraeus-Lindqvist and plasma skimming effects consist of nonlinear expressions. The iterative approach described in section 3.2.2 is applied here and the linear system described above is solved once for every iteration.

Figure 8 shows the main outputs of the model. On the top left panel we see that the pressure in the network progressively decreases from the arteriolar to the venular ends of the microvasculature, as expected. The blood velocity (shown in the top right panel), however, is not uniformly distributed and several network branches are crossed by a flow rate significantly lower than the average (i.e. the dark blue color).

Concerning the interaction of the microvasculature with the interstitial flow, we observe that the variation of pressure through the capillary bed influences the pressure in the interstitial space. This is shown in the middle left panel, by the slice of the interstitial pressure field. We see that in proximity of the arteriolar end of the network, an increased interstitial pressure level is visible, while it decreases below average next to the venules. Then, it is apparent that the pressure gradient in the vasculature induces a secondary, weaker gradient in the interstitium. This effect generates a modest flow in the interstitial volume, which is clearly visible in the middle right panel. On the bottom row of the figure we show the viscosity and the hematocrit. We notice that the hematocrit is characterized by a high spatial variability, while the changes of apparent viscosity are less spread, in line with the observations of Figure 5.

5. DISCUSSION

The results of Section 4 show that the proposed computational approach is correct if compared to idealized tests with analytical solutions and it also captures the main traits of microcirculation in more complex cases, such as the one addressed in 4.3.2. However, performing a detailed validation of the model is a very difficult task.

Concerning the vascular network, local measurements are very challenging because of the small size of the capillaries and the intrinsic variability of the network morphology. We refer for example to [30] where capillary flow velocity measurements in vivo and in situ are provided, and we observe that the reported range of velocities is compatible with the ones computed in Figure 8. Comparable results with those of Figure 8 are also shown in [57] for the distribution of velocities. Unfortunately, we are not yet aware of local measurements of hematocrit and viscosity, which could allow us to validate the predictions of the model for these quantities.

Concerning the interstitial volume and the fluid balance between this region and the capillary bed, the mean interstitial pressure is a model output for which measurements are more easily available. For example a detailed study where the model predictions and measurements available in the literature were compared was recently performed by the authors in [47]. There, the authors have used the model for the analysis of microvascular fluid balance. For this reason, model was complemented by new specific features addressing the lymphatic drainage. The results of that study show that the model matches well with the available data in the literature for the interstitial fluid pressure and net filtration rate. For the first indicator, the values predicted by the model agree with those reported in [12], where for healthy volunteers an interstitial pressure of $-0.9 \pm 1.3 \ mmHg$ is observed in vivo. In addition, when the pathological conditions of uremic patients were simulated,

interstitial fluid pressure increased, in agreement with the range of $4.6 \pm 4.2 \ mmHg$ reported in [12]. Therefore, the variation of interstitial pressure is correctly reproduced by the model according to physiological evidence. The net filtration rate is the integral along the microvascular network of the net fluid flow from the capillaries to the interstitial volume, namely $\int_\Lambda 2\pi R_i(s) f(\overline{\overline{p}}_t(s), \overline{p}_v(s)) ds$. For comparison with available measurements, the result of this formula is rescaled to the whole extra-vascular volume in the body [25]. More precisely, the value reported for the entire body is about $2 \ ml/min$ [25], which is in agreement with the prediction of $1.96 \ ml/min$ obtained by the authors in [47].

Thanks to the unique ability to model local microvascular flow, combined with fluid balance with the tissue interstitium, the computational model can be adopted to study various applications where microcirculation plays a fundamental role. Among these we mention the study of vascularized tumors and in particular the simulation of the tumor microenvironment. Indeed, authors and co-workers have applied a simplified version of this model, where blood flow was modeled using a constant viscosity, to simulate and compare different drug delivery therapies, see [6, 5, 42, 43], based on mass and heat transport superposed to microcirculation. Considering the increasing interest in the application of sophisticated mathematical models to study the fluid and tissue mechanics in the brain, see for example [53, 27, 41, 64], we see a significant potential in the application of the proposed model to analyze the interaction of vasculature and cerebrospinal fluid for metabolic waste clearance in the brain, according to the mechanisms hypothesized in [29].

Although the computational model seems to be a valuable complementary tool to experimental research in biology and medicine, it is still affected by several limitations. First of all, working at small space scales, we have to face a significant variability of the tissue properties and in the morphology of the network. Indeed, the simulation of section 4.3.2, is just a single occurrence of many possibilities characterized by a probability distribution. In this context, the numerical simulations shall be rather used within a statistical framework, in order to determine the mean values and the variance of some specific quantities of interest related to microcirculation. If applied to the morphology of the microvasculature, this becomes a particularly challenging issue. In fact, it is known that morphology of capillary networks strongly depends on the host organ and type of tissue (see for example [48]). In some cases, such as the healthy muscle tissue and particularly when arteriole and venulae are included, a tree like structure is apparent. To model pathological situations, such as the ones occurring in tumors, a network like configuration of the capillary bed (such as the one of Figure 7) is preferred instead, as discussed in [18, 21]. The proposed computational approach is completely general with respect to the morphology of the network. In this respect, the simulations of section 4.3.2 are just an example among many other studies that will be performed.

Second, we observe that the interaction of the tissue sample with the surrounding system is described by rather coarse approximations. Coupling the current model with other ones that account for flow at the systemic level will be a future direction of improvement. This can be achieved by making the boundary conditions of the model become dependent of a macroscale approximation of the systemic circulation, based on lumped parameter models inspired to the analogy between the vascular system and electrical circuits, see for example [66]. Furthermore, these models should be also complemented by equations that describe the mass and heat metabolism at the systemic level (due to the systemic circulation, the lymphatic system, the bio-heat transfer for temperature regulation etc.)

Finally, despite the model framework is rigorously derived from the governing principles of flow and transport, the nonlinear blood rheology is still determined by a phenomenological process. However, the model is completely general with respect to rheology. If a more advanced rheology was available, perhaps by means of a multiscale approach, the current model could easily be updated to incorporate it. Indeed, a one-way multiscale approach for blood rheology is currently under development by the research team and co-workers [34]. In particular, microscale effects are incorporated in the model by studying individual red blood cells flowing at different Reynolds numbers and different levels of hematocrit. In this way, we will replace expression (9) with a new one derived upon mechanistic principles.

6. CONCLUSIONS, LIMITATIONS AND PRESPECTIVES

We have derived a mathematical model that encompasses nonlinear blood rheology (Fahraeus-Lindqvist and plasma skimming effects), capillary leakage and flow in the interstitial volume for a microvascular network of possibly curved vessels. Numerical tests have confirmed that all these features play a role in microcirculation. Furthermore, thanks to a sophisticated mathematical formulation complemented by advanced numerical solvers that discretize partial differential equations defined in one-dimension (for the network) and three-dimensions (for the interstitial volume), we are able to apply the model to fairly complex network configurations. The results obtained by the model are quantitatively consistent with the physiological values expected for healthy cases.

Concerning applications, we believe that the model is a flexible tool of investigation to be used in may areas of research of medicine and biology, such as oncology, neurology and nephrology. For example, the authors and co-workers have used previous versions of it to study drug delivery to the

tumor microenvironment [6, 5, 43, 42]. The current model is being used by the authors to analyze the effect of lymphatic drainage in uremic patients [47].

A. THE EQUATIONS SOLVED FOR FLOW AND HEMATOCTIT

For the sake of clarity and to foster the reproducibility and verifiability of the results, we derive here the algebraic form of the discrete problem. These equations are implemented and solved using a software based on the finite element library Getfem++ [17].

Let us start by defining some notation for the application of the finite element method. Let us first introduce the dimension of the finite element spaces:

$$N_t^h := \dim\left(\boldsymbol{V}_t^h\right),\ M_t^h := \dim\left(Q_t^h\right),\ N_v^h := \dim\left(V_v^h\right),\ M_v^h := \dim\left(Q_v^h\right),\ S_v^h := \dim\left(W_v^h\right).$$

Since the tissue 3D and the vessel 1D meshes are independent, we define three sets, containing respectively the finite element basis for $\boldsymbol{V}_t^h \times Q_t^h$, $V_v^h \times Q_v^h$ and W_v^h:

$$\left\{\boldsymbol{\varphi}_t^i\right\}_{i=1}^{N_t^h} \times \left\{\psi_t^i\right\}_{i=1}^{M_t^h}, \qquad \left\{\varphi_v^i\right\}_{i=1}^{N_v^h} \times \left\{\psi_v^i\right\}_{i=1}^{M_v^h}, \qquad \left\{\phi_v^i\right\}_{i=1}^{S_v^h}.$$

Then, we express our variables as linear combination of the basis elements as follows:

$$\boldsymbol{u}_t^h\left(\mathbf{x}\right) = \sum_{i=1}^{N_t^h} U_t^i\,\boldsymbol{\varphi}_t^i\left(\mathbf{x}\right),\ p_t^h\left(\mathbf{x}\right) = \sum_{i=1}^{M_t^h} P_t^i\,\psi_t^i\left(\mathbf{x}\right),\ \forall\,\mathbf{x} \in \Omega, \tag{22}$$

$$u_v^h\left(s\right) = \sum_{i=1}^{N_v^h} U_v^i\,\varphi_v^i\left(s\right),\ p_v^h\left(s\right) = \sum_{i=1}^{M_v^h} P_v^i\,\psi_v^i\left(s\right),\ \forall\,s \in \Lambda, \tag{23}$$

$$H^h\left(s\right) = \sum_{i=1}^{S_v^h} H^i\,\phi_v^i\left(s\right),\ \forall\,s \in \Lambda, \tag{24}$$

being $\mathbf{U}_t = \left\{U_t^i\right\}_{i=1}^{N_t^h}$, $\mathbf{P}_t = \left\{P_t^i\right\}_{i=1}^{M_t^h}$, $\mathbf{U}_v = \left\{U_v^i\right\}_{i=1}^{N_v^h}$, $\mathbf{P}_v = \left\{P_v^i\right\}_{i=1}^{M_v^h}$ and $\mathbf{H} = \left\{H^i\right\}_{i=1}^{S_v^h}$ the vectors containing the degrees of freedom of the finite elements approximations. Now using the

linearity of the operators, we rewrite (19) in algebraic form:

$$
\begin{bmatrix}
\mathbb{M}_{tt} & -\mathbb{D}_{tt}^T & \mathbb{O} & \mathbb{O} \\
\mathbb{D}_{tt} & \mathbb{B}_{tt} & \mathbb{O} & -\mathbb{B}_{tv} \\
\mathbb{O} & \mathbb{O} & \mathbb{M}_{vv} & -\mathbb{D}_{vv}^T - \mathbb{J}_{vv}^T \\
\mathbb{O} & -\mathbb{B}_{vt} & \mathbb{D}_{vv} + \mathbb{J}_{vv} & \mathbb{B}_{vv}
\end{bmatrix}
\begin{bmatrix}
\mathbf{U}_t \\
\mathbf{P}_t \\
\mathbf{U}_v \\
\mathbf{P}_v
\end{bmatrix}
=
\begin{bmatrix}
\mathbf{F}_t \\
-\mathbb{B}_{tt}\delta\pi \\
\mathbf{F}_v \\
\mathbb{B}_{vv}\delta\pi
\end{bmatrix}
\tag{25}
$$

$$
\left[\mathbb{B}_h + \mathbb{J}_h + \mathbb{O}_h\right]\left[\mathbf{H}\right] = \left[\mathbf{F}_h\right]
\tag{26}
$$

which correspond to the equations solved for the fluid mechanics problem (previously also represented as $[\boldsymbol{u}_t^h, u_v^h, p_t^h, p_v^h] = \mathcal{F}^h(\mu_v)$) and for the hematocrit problem (that was represented as $H^h = \mathcal{H}^h(u_v^h)$). The matrices of the previous system are calculated as follows, using suitable numerical integration formulas, starting from the bilinear forms (more generally, the mathematical operators) of problem (19):

$$[\mathbb{M}_{tt}]_{ij} := (\frac{\mu_t}{K_t}\boldsymbol{\varphi}_t^j, \boldsymbol{\varphi}_t^i)_\Omega \qquad\qquad \mathbb{M}_{tt} \in \mathbb{R}^{N_t^h \times N_t^h},$$

$$[\mathbb{D}_{tt}]_{ij} := (\nabla \cdot \boldsymbol{\varphi}_t^j, \psi_t^i)_\Omega \qquad\qquad \mathbb{D}_{tt} \in \mathbb{R}^{N_t^h \times M_t^h},$$

$$[\mathbb{B}_{tt}]_{ij} := (2\pi R L_p \overline{\overline{\psi}}_t^j \delta_{\Lambda_h}, \psi_t^i)_\Omega \qquad\qquad \mathbb{B}_{tt} \in \mathbb{R}^{M_t^h \times M_t^h},$$

$$[\mathbb{B}_{tv}]_{ij} := (2\pi R L_p \overline{\psi}_v^j \delta_{\Lambda_h}, \psi_t^i)_\Omega \qquad\qquad \mathbb{B}_{tv} \in \mathbb{R}^{M_t^h \times M_v^h},$$

$$[\mathbb{B}_{vt}]_{ij} := (2\pi R L_p \overline{\overline{\psi}}_t^j, \psi_v^i)_\Lambda \qquad\qquad \mathbb{B}_{vt} \in \mathbb{R}^{M_v^h \times M_t^h},$$

$$[\mathbb{B}_{vv}]_{ij} := (2\pi R L_p \overline{\psi}_v^j, \psi_v^i)_\Lambda \qquad\qquad \mathbb{B}_{vv} \in \mathbb{R}^{M_v^h \times M_v^h},$$

$$[\mathbb{M}_{vv}]_{ij} := (-2\pi \mu_{v,i}\phi'(1)\big(1 + \kappa_i^2 R_i^2\big)\pi R_i^2 \overline{\varphi}_v^j, \varphi_v^i) \qquad\qquad \mathbb{M}_{vv} \in \mathbb{R}^{N_v^h \times N_v^h},$$

$$[\mathbb{D}_{vv}]_{ij} := (\pi R^2 \partial \overline{\varphi}_v^j, \psi_v^i)_\Lambda \qquad\qquad \mathbb{D}_{vv} \in \mathbb{R}^{N_v^h \times M_v^h},$$

$$[\mathbb{J}_{vv}]_{ij} := \langle \varphi_v^j, \overline{\psi}_v^i \rangle_J \qquad\qquad \mathbb{J}_{vv} \in \mathbb{R}^{N_v^h \times M_v^h},$$

$$[\mathbf{F}_t]_i := -(g_t^h, \boldsymbol{\varphi}_t^i \cdot \mathbf{n})_{\Gamma_p} \qquad\qquad \mathbf{F}_t \in \mathbb{R}^{N_t^h},$$

$$[\mathbf{F}_v]_i := -\sum_{i \in \mathcal{B}} \left[g_v^+ \, \pi R_i^2 v_v^h|_{\boldsymbol{x}_i^+} - g_v^- \, \pi R_i^2 v_v^h|_{\boldsymbol{x}_i^-} \right] \qquad\qquad \mathbf{F}_v \in \mathbb{R}^{N_v^h},$$

$$[\mathbb{B}_h]_{i,j} := \left(\pi R_i^2 \overline{u}_{v,p} \varphi^p \phi_j \,,\, \partial_s \phi_i \right)_\Lambda \qquad\qquad \mathbb{B}_h \in \mathbb{R}^{S_v^h},$$

$$[\mathbb{J}_h]_{i,j} := \langle\langle \phi_v^j, \phi_v^i \rangle\rangle_{in} \qquad\qquad \mathbb{J}_h \in \mathbb{R}^{S_v^h},$$

$$[\mathbb{O}_h]_{i,j} := \langle\langle \phi_h^j \phi_h^i \rangle\rangle_{out} \qquad\qquad \mathbb{O}_h \in \mathbb{R}^{S_v^h},$$

$$[\mathbf{F}_h]_i := \sum_{k \in \mathcal{B}} \pi R_k^2 \overline{u}_{v,k}^h H_0 w_k^h|_{\boldsymbol{x}_k^{in}} \qquad\qquad \mathbf{F}_h \in \mathbb{R}^{S_v^h}.$$

For simplicity we have introduced the compact notation $\langle \cdot, \cdot \rangle_J$, $\langle\langle H^h, w^h \rangle\rangle_{out}$, $\langle\langle H^h, w^h \rangle\rangle_{in}$, to indicate the junction, inflow and outflow terms of problem (19), respectively,

$$\left\langle q_v^h, \overline{u}_v^h \right\rangle_J := \sum_j q_v^h|_{\boldsymbol{y}_j} \left[\sum_{i \in \mathcal{K}_j^+} \pi R_i^2 \overline{u}_{v,i}^h|_{\boldsymbol{y}_j} - \sum_{i \in \mathcal{K}_j^-} \pi R_i^2 \overline{u}_{v,i}^h|_{\boldsymbol{y}_j} \right],$$

$$\langle\langle H^h, w^h \rangle\rangle_{out} := \sum_j \sum_{i \in \mathcal{K}^{out}} \pi R_i^2 \overline{u}_{v,i}^h H_i^h w_i^h|_{\boldsymbol{y}_j} + \sum_{i \in \mathcal{B}} \pi R_i^2 \overline{u}_{v,i}^h H_i^h w_i^h|_{\boldsymbol{x}_i^{out}} + \sum_{i \in \mathcal{E}} \pi R_i^2 \overline{u}_{v,i}^h H_i^h w_i^h|_{\boldsymbol{z}_i},$$

$$\langle\langle H^h, w^h \rangle\rangle_{in} := -\sum_j \sum_{i \in \mathcal{K}_j^{in}} F_{QE,j,i} w_i^h|_{\boldsymbol{y}_j} \left(\sum_{i \in \mathcal{K}_j^{out}} \pi R_i^2 \overline{u}_{v,i}^h H_i^h|_{\boldsymbol{y}_j} \right).$$

REFERENCES

1. L.T. Baxter and R.K. Jain. Transport of fluid and macromolecules in tumors. ii. role of heterogeneous perfusion and lymphatics. *Microvascular Research*, 40(2):246–263, 1990.

2. Franco Brezzi and Michel Fortin. *Mixed and hybrid finite element methods*, volume 15 of *Springer Series in Computational Mathematics*. Springer-Verlag, New York, 1991.

3. Russell T Carr and Jewen Xiao. Plasma Skimming in Vascular Trees: Numerical Estimates of Symmetry Recovery Lengths. *Microcirculation*, 2(4):345–353, jan 1995.

4. Francis Cassot, Frederic Lauwers, Sylvie Lorthois, Prasanna Puwanarajah, Valérie Cances-Lauwers, and Henri Duvernoy. Branching patterns for arterioles and venules of the human cerebral cortex. *Brain Research*, 1313:62–78, 2010.

5. L. Cattaneo and P. Zunino. A computational model of drug delivery through microcirculation to compare different tumor treatments. *International Journal for Numerical Methods in Biomedical Engineering*, 30(11):1347–1371, 2014.

6. L. Cattaneo and P. Zunino. Computational models for fluid exchange between microcirculation and tissue interstitium. *Networks and Heterogeneous Media*, 9(1):135–159, 2014.

7. Laura Cattaneo and Paolo Zunino. Computational models for fluid exchange between microcirculation and tissue interstitium. *Networks and Heterogeneous Media*, 9(1):135–159, 2014.

8. Radomir Chabiniok, Vicky Y. Wang, Myrianthi Hadjicharalambous, Liya Asner, Jack Lee, Maxime Sermesant, Ellen Kuhl, Alistair A. Young, Philippe Moireau, Martyn P. Nash, Dominique Chapelle, and David A. Nordsletten. Multiphysics and multiscale modelling, data–model fusion and integration of organ physiology in the clinic: ventricular cardiac mechanics. *Interface Focus*, 6(2), 2016.

9. C. D'Angelo. *Multi scale modelling of metabolism and transport phenomena in living tissues, PhD Thesis*. EPFL, Lausanne, 2007.

10. C. D'Angelo. Finite element approximation of elliptic problems with dirac measure terms in weighted spaces: Applications to one- and three-dimensional coupled problems. *SIAM Journal on Numerical Analysis*, 50(1):194–215, 2012.

11. C. D'Angelo and A. Quarteroni. On the coupling of 1d and 3d diffusion-reaction equations. application to tissue perfusion problems. *Mathematical Models and Methods in Applied Sciences*, 18(8):1481–1504, 2008.

12. Leonard M Ebah, Helge Wiig, Idalia Dawidowska, Charlotte O'Toole, Angela Summers, Milind Nikam, Anuradha Jayanti, Beatrice Coupes, Paul Brenchley, and Sandip Mitra. Subcutaneous interstitial pressure and volume characteristics in renal impairment associated with edema. *Kidney international*, 84(5):980–8, 2013.

13. D.A. Fedosov, B. Caswell, A.S. Popel, and G.E.M. Karniadakis. Blood flow and cell-free layer in microvessels. *Microcirculation*, 17(8):615–628, 2010.

14. D.A. Fedosov, W. Pan, B. Caswell, G. Gompper, and G.E. Karniadakis. Predicting human blood viscosity in silico. *Proceedings of the National Academy of Sciences of the United States of America*, 108(29):11772–11777, 2011.

15. Gregory J. Fleischman, Timothy W. Secomb, and Joseph F. Gross. Effect of extravascular pressure gradients on capillary fluid exchange. *Mathematical Biosciences*, 81(2):145–164, 1986.

16. Gregory J. Fleischman, Timothy W. Secomb, and Joseph F. Gross. The interaction of extravascular pressure fields and fluid exchange in capillary networks. *Mathematical Biosciences*, 82(2):141–151, 1986.

17. Michel Fournié, Nicolas Renon, Yves Renard, and Daniel Ruiz. Cfd parallel simulation using getfem++ and mumps. In Pasqua D'Ambra, Mario Guarracino, and Domenico Talia, editors, *Euro-Par 2010 - Parallel Processing*, pages 77–88, Berlin, Heidelberg, 2010. Springer Berlin Heidelberg.

18. Graham M. Fraser, Daniel Goldman, and Christopher G. Ellis. Microvascular Flow Modeling using In Vivo Hemodynamic Measurements in Reconstructed 3D Capillary Networks. *Microcirculation*, 19(6):510–520, 2012.

19. Brendan C. Fry, Jack Lee, Nicolas P. Smith, and Timothy W. Secomb. Estimation of Blood Flow Rates in Large Microvascular Networks. *Microcirculation*, 19(6):530–538, 2012.

20. Louis Gagnon, Amy F. Smith, David A. Boas, Anna Devor, Timothy W. Secomb, and Sava Sakadžić. Modeling of Cerebral Oxygen Transport Based on In vivo Microscopic Imaging of Microvascular Network Structure, Blood Flow, and Oxygenation. *Frontiers in Computational Neuroscience*, 10(August):82, 2016.

21. Y. Gazit, J.W. Baish, N. Safabakhsh, M. Leunig, L.T. Baxter, and R.K. Jain. Fractal characteristics of tumor vascular architecture during tumor growth and regression. *Microcirculation*, 4(4):395–402, 1997.

22. Daniel Goldman and Aleksander S Popel. A Computational Study of the Effect of Capillary Network Anastomoses and Tortuosity on Oxygen Transport. *Journal of Theoretical Biology*, 206(2):181–194, 2000.

23. Ian G. Gould and Andreas A. Linninger. Hematocrit Distribution and Tissue Oxygenation in Large Microcirculatory Networks. *Microcirculation*, 22(1):1–18, jan 2015.

24. A C Guyton, H J Granger, and A E Taylor. Interstitial fluid pressure. *Physiological reviews*, 51(3):527–63, jul 1971.

25. Arthur C. Guyton and John E Hall. *Guyton and Hall Textbook of Medical Physiology 13th edition*. Number 1. Philadelphia, 13th edition, 2015.

26. John M. Higgins, David T. Eddington, Sangeeta N. Bhatia, and L. Mahadevan. Statistical dynamics of flowing red blood cells by morphological image processing. *PLoS Computational Biology*, 5(2), 2009.

27. K.E. Holter, B. Kehlet, A. Devor, T.J. Sejnowski, A.M. Dale, S.W. Omholt, O.P. Ottersen, E.A. Nagelhus, K.-A. Mardal, and K.H. Pettersen. Interstitial solute transport in 3d reconstructed neuropil occurs by diffusion rather than bulk flow. *Proceedings of the National Academy of Sciences of the United States of America*, 114(37):9894–9899, 2017.

28. Richard Hsu and Timothy W. Secomb. A Green's function method for analysis of oxygen delivery to tissue by microvascular networks. *Mathematical Biosciences*, 96(1):61–78, 1989.

29. Jeffrey J. Iliff, Minghuan Wang, Yonghong Liao, Benjamin A. Plogg, Weiguo Peng, Georg A. Gundersen, Helene Benveniste, G. Edward Vates, Rashid Deane, Steven A. Goldman, Erlend A. Nagelhus, and Maiken Nedergaard. A Paravascular Pathway Facilitates CSF Flow Through the Brain Parenchyma and the Clearance of Interstitial Solutes, Including Amyloid β. *Science translational medicine*, 4(147):147ra111, 2012.

30. M. Intaglietta, N.R. Silverman, and W.R. Tompkins. Capillary flow velocity measurements in vivo and in situ by television methods. *Microvascular Research*, 10(2):165 – 179, 1975.

31. T. Köppl and B. Wohlmuth. Optimal a priori error estimates for an elliptic problem with dirac right-hand side. *SIAM Journal on Numerical Analysis*, 52(4):1753–1769, 2014.

32. M. Kuchta, M. Nordaas, J.C.G. Verschaeve, M. Mortensen, and K.-A. Mardal. Preconditioners for saddle point systems with trace constraints coupling 2d and 1d domains. *SIAM Journal on Scientific Computing*, 38(6):B962–B987, 2016.

33. E.M. Landis and J.R. Pappenheimer. Exchange of substances through the capillary walls. In W. F. Hamilton, editor, *Handbook of Physiology. Circulation*, chapter 29, pages 961–1034. Am. Physiol. Soc., Washington, DC, 1963.

34. F. Laurino, A. Coclite, A. Tiozzo, P. Decuzzi, and P. Zunino. A multiscale computational approach for the interaction of functionalized nanoparticles with the miscrovasculature. Technical report, Politecnico di Milano, 2018.

35. Jack Lee and Nicolas P. Smoth. Theoretical modeling in hemodynamics of microcirculation. *Microcirculation*, 15(8):699–714, 2008.

36. J R Levick. Capillary filtration-absorption balance reconsidered in light of dynamic extravascular factors. *Experimental physiology*, 76:825–857, 1991.

37. E.K. Lindstrom, J. Schreiner, G.A. Ringstad, V. Haughton, P.K. Eide, and K.-A. Mardal. Comparison of phase-contrast mr and flow simulations for the study of csf dynamics in the cervical spine. *Neuroradiology Journal*, 2018.

38. A. A. Linninger, I. G. Gould, T. Marinnan, C.-Y. Hsu, M. Chojecki, and A. Alaraj. Cerebral Microcirculation and Oxygen Tension in the Human Secondary Cortex. *Annals of Biomedical Engineering*, 41(11):2264–2284, nov 2013.

39. Adrien Lucker, Timothy W. Secomb, Bruno Weber, and Patrick Jenny. The relative influence of hematocrit and red blood cell velocity on oxygen transport from capillaries to tissue. *Microcirculation*, 24(3):e12337–n/a, 2017. e12337.

40. B J Mcguire and T W Secomb. Based on Maximal Oxygen Consumption Rates. 5051:2382–2391, 2003.

41. L.A. Mihai, S. Budday, G.A. Holzapfel, E. Kuhl, and A. Goriely. A family of hyperelastic models for human brain tissue. *Journal of the Mechanics and Physics of Solids*, 106:60–79, 2017.

42. M. Nabil, P. Decuzzi, and P. Zunino. Modelling mass and heat transfer in nano-based cancer hyperthermia. *Royal Society Open Science*, 2(10), 2015.

43. Mahdi Nabil and Paolo Zunino. A computational study of cancer hyperthermia based on vascular magnetic nanoconstructs. *Royal Society Open Science*, 3(9), 2016.

44. Domenico Notaro, Laura Cattaneo, Luca Formaggia, Anna Scotti, and Paolo Zunino. A mixed finite element method for modeling the fluid exchange between microcirculation and tissue interstitium. In Giulio Ventura and Elena Benvenuti, editors, *Advances in Discretization Methods: Discontinuities, Virtual Elements, Fictitious Domain Methods*, pages 3–25. Springer International Publishing, Cham, 2016.

45. Dominik Obrist, Bruno Weber, Alfred Buck, and Patrick Jenny. Red blood cell distribution in simplified capillary networks. *Phil. Trans. R. Soc. A*, 368:2897–2918, 2010.

46. D. Pinho, R. Lima, A. I. Pereira, and F. Gayubo. Tracking Red Blood Cells in Microchannels: A Comparative Study Between an Automatic and a Manual Method. pages 165–180. 2013.

47. L. Possenti, G. Casagrande, S. Di Gregorio, M.L. Costantino, and P. Zunino. A finite element model of vascular fluid balance at the microscale: influence of a non-linear model of lymphatics. Technical report, Politecnico di Milano, 2018.

48. C. Pozrikidis. Numerical simulation of blood flow through microvascular capillary networks. *Bulletin of Mathematical Biology*, 71(6):1520–1541, 2009.

49. A R Pries and T W Secomb. Microvascular blood viscosity in vivo and the endothelial surface layer. *American journal of physiology. Heart and circulatory physiology*, 289(6):H2657–H2664, 2005.

50. A R Pries, T W Secomb, T. Gessner, M B Sperandio, J F Gross, and P Gaehtgens. Resistance to blood flow in microvessels in vivo. *Circulation Research*, 75(5):904–915, nov 1994.

51. Alfio Quarteroni and Alberto Valli. *Numerical approximation of partial differential equations*, volume 23 of *Springer Series in Computational Mathematics*. Springer-Verlag, Berlin, 1994.

52. Johannes Reichold, Marco Stampanoni, Anna Lena Keller, Alfred Buck, Patrick Jenny, and Bruno Weber. Vascular graph model to simulate the cerebral blood flow in realistic vascular networks. *Journal of cerebral blood flow and metabolism : official journal of the International Society of Cerebral Blood Flow and Metabolism*, 29(8):1429–1443, 2009.

53. G. Ringstad, E.K. Lindstrm, S.A.S. Vatnehol, K.-A. Mardal, K.E. Emblem, and P.K. Eide. Non-invasive assessment of pulsatile intracranial pressure with phase-contrast magnetic resonance imaging. *PLoS ONE*, 12(11), 2017.

54. N. Safaeian and T. David. A computational model of oxygen transport in the cerebrocapillary levels for normal and pathologic brain function. *Journal of Cerebral Blood Flow and Metabolism*, 33(10):1633–1641, 2013.

55. N. Safaeian, M. Sellier, and T. David. A computational model of hemodynamic parameters in cortical capillary networks. *Journal of Theoretical Biology*, 271(1):145–156, 2011.

56. T W Secomb, D A Beard, J C Frisbee, N P Smith, and A R Pries. The role of theoretical modeling in microcirculation research. *Microcirculation*, 15(8):693–698, 2008.

57. Timothy W. Secomb. A green's function method for simulation of time-dependent solute transport and reaction in realistic microvascular geometries. *Mathematical Medicine and Biology: A Journal of the IMA*, 33(4):475–494, 2016.

58. Timothy W Secomb. Blood Flow in the Microcirculation. *Annu. Rev. Fluid Mech*, 49(August):443–61, 2017.

59. DU Silverthorn. *Human Physiology*. 2010.

60. Melody A. Swartz and Mark E. Fleury. Interstitial Flow and Its Effects in Soft Tissues. *Annual Review of Biomedical Engineering*, 9(1):229–256, 2007.

61. P.W. Sweeney, S. Walker-Samuel, and R.J. Shipley. Insights into cerebral haemodynamics and oxygenation utilising in vivo mural cell imaging and mathematical modelling. *Scientific Reports*, 8(1), 2018.

62. B. Wohlmuth P. Zunino T. Koeppl, E. Vidotto. Mathematical modelling, analysis and numerical approximation of second order elliptic problems with inclusions. *Mathematical Models and Methods in Applied Sciences*, 28(05), 2018.

63. B. Tully and Y. Ventikos. Cerebral water transport using multiple-network poroelastic theory: application to normal pressure hydrocephalus. *Journal of Fluid Mechanics*, 667:188215, 2011.

64. J. Weickenmeier, P. Saez, C.A.M. Butler, P.G. Young, A. Goriely, and E. Kuhl. Bulging brains. *Journal of Elasticity*, 129(1-2):197–212, 2017.

65. Michael Welter and Heiko Rieger. Interstitial Fluid Flow and Drug Delivery in Vascularized Tumors: A Computational Model. *PLoS ONE*, 8(8), 2013.

66. Nico Westerhof, Jan-Willem Lankhaar, and Berend E. Westerhof. The arterial windkessel. *Medical & Biological Engineering & Computing*, 47(2):131–141, Feb 2009.